Plasmonic Photocatalysts Based on Au Nanoparticles and WO3 for Visible Light-Induced Photocatalytic Activity

Margaux Desseigne, Virginie Chevallier, Véronique Madigou, Marie-Vanessa Coulet, Olivier Heintz, Hassan Ait Ahsaine, Madjid Arab

catalysts

MDPI

Article

Plasmonic Photocatalysts Based on Au Nanoparticles and WO_3 for Visible Light-Induced Photocatalytic Activity

Margaux Desseigne [1], Virginie Chevallier [1], Véronique Madigou [1], Marie-Vanessa Coulet [2], Olivier Heintz [3], Hassan Ait Ahsaine [4] and Madjid Arab [1,*]

[1] Aix Marseille Université, Université de Toulon CNRS, IM2NP, CS 60584, CEDEX 9, F-83041 Toulon, France; margaux.desseigne@univ-tln.fr (M.D.); virginie.chevallier@univ-tln.fr (V.C.); madigou@univ-tln.fr (V.M.)
[2] Aix-Marseille Université, CNRS, MADIREL (UMR 7246), Campus de St Jérôme, 13013 Marseille, France
[3] Laboratoire Interdisciplinaire Carnot de Bourgogne (UMR 6303 CNRS), Université de Bourgogne Franche-Comté, F-21078 Dijon, France; olivier.heintz@u-bourgogne.fr
[4] Laboratoire de Chimie Appliquée des Matériaux, Faculté des Sciences, Mohammed V University in Rabat, Rabat B.P. 1014, Morocco; h.aitahsaine@um5r.ac.ma
* Correspondence: madjid.arab@univ-tln.fr

Abstract: In this work, we report the application of Au/WO_3 composite as a photocatalyst for the degradation of dyes under solar light irradiation. Au/WO_3 nanocomposites were synthesized using an acid precipitation method followed by an impregnation/reduction at room temperature. Two composites were obtained by loading gold nanoparticles on two morphologies of nanostructured WO_3, nanoplatelets (NP), and pseudospheres (PS). The elaboration parameters of the nanocomposites were optimized according to the gold mass percentage, the $HAuCl_4$ precursor concentration, and the impregnation time. The structural, microstructural, and textural characterization were conducted using advanced techniques: XRD, SEM/TEM microscopies, and XPS and DRS spectroscopies. The optimal synthesis parameters are a 48 h impregnation of a five mass percentage of gold from a $HAuCl_4$ precursor with a concentration of 10^{-3} mol·L^{-1}. The obtained composites were formed with Au nanoparticles of 7 nm in size. The XRD analyses did not reveal any modification of the oxide supports structure after gold grafting, contrary to the sorption analyses, which evidenced a change in the state of the materials surface. XPS analysis revealed the reduction of W^{6+} ions into W^{5+}, favoring the presence of oxygen vacancies. Furthermore, a localized surface plasmon resonance effect was observed in the composite at 540 nm. The photocatalysis results of several dye pollutants have shown a selective degradation efficiency depending on the charge of the polluting molecules, pH medium, and mass loading of the catalysts. At the native pH, the photocatalysis process is highly efficient on a cationic molecule, with a low adsorption capacity. Au/WO_3 PS composite appears to be the most efficient, degrading almost the whole RhB and MB only in 60 min and 90 min, respectively, while, for the MO anionic dye, the degradation is more efficient in acidic medium (80%) than in basic medium (0%). Trap tests of the main active species were investigated and a photodecomposition mechanism is proposed.

Keywords: hybrid nanomaterials; composite; morphology; LSPR effect; dyes degradation

Citation: Desseigne, M.; Chevallier, V.; Madigou, V.; Coulet, M.-V.; Heintz, O.; Ait Ahsaine, H.; Arab, M. Plasmonic Photocatalysts Based on Au Nanoparticles and WO_3 for Visible Light-Induced Photocatalytic Activity. *Catalysts* **2023**, *13*, 1333. https://doi.org/10.3390/catal13101333

Academic Editor: Bo Weng

Received: 24 July 2023
Revised: 19 September 2023
Accepted: 26 September 2023
Published: 29 September 2023

1. Introduction

Among the countless substances that pollute aquatic environments and drinking water, certain worrying contaminants are the focus of the scientific community's efforts because of their non-biodegradable nature and toxicity. Most organic dyes used in paper manufacturing, textile dyeing, or the paint, cosmetics and food industries [1–3] may be partially hydrolyzed [4]. However, their by-products contain aromatic and heterocyclic rings, making them highly toxic, mutagenic or carcinogenic, and persistent.

Conventional physical and chemical water treatment methods remain ineffective for from 10% to 15% of the 10,000 types of dyes discharged by various industries [4,5]. They

merely convert these pollutants from one oxidation state to another, a process known as photobleaching.

In contrast, advanced oxidation processes are seen as promising potential techniques for the treatment of wastewater polluted by hazardous organic dyes, more specifically, heterogeneous photocatalytic degradation.

The principle of this method is based on the combined use of a specific material, the photocatalyst, and sufficiently energetic radiation to break down pollutants into less toxic or non-toxic components. Provided it is conducted under natural sunlight, photocatalytic degradation is a cost-effective, environmentally friendly technology that works at an ambient pressure and temperature, enabling complete mineralization of the dye (conversion to water and CO_2) [6–9].

Semiconductors are among the most efficient materials for photocatalytic degradation. They are capable of generating reactive oxygen species (ROS) with high oxidation potentials—hydroxyl radicals, $^{\bullet}OH$; superoxide anion, $^{\bullet}O^{2-}$; and hydrogen peroxide, H_2O_2—after excitation by suitable radiation. Yet, most conventionally used semiconductors are photoactive only in the UV region, leaving the visible range spectrum unused. This is why various strategies have been developed to enhance their optical properties and design photocatalysts with tunable bandgaps. This involves modifying various properties such as their shape, size, crystalline phase, porosity, and surface state, which influence their bandgap, their specific surface area, and the density or nature of the adsorption sites [10].

In parallel, new semiconductors with narrower band gaps have also been studied. Among them, WO_3, an n-type semiconductor, has proven particularly interesting, with its bandgap being tunable between 2.4 and 3.0 eV, depending on its structure, morphology, or stoichiometry. As a result, it exhibits high photoactivity under solar irradiation, thanks also to its deep valence band, its high capacity to absorb visible light, and the high oxidizing ability of the holes in its valence band.

Despite its visible light response, pure WO_3 has two main disadvantages: a fast recombination rate of photogenerated electrons/holes and a low conduction band (CB) edge position [11,12]. Because of its positive (ca. +0.5 eV vs. NHE) CB edge compared to the reduction potential of O_2 (i.e., $O_2/O_2^- = -0.33$ V vs. NHE), WO_3 is inefficient to carry out a reduction process in any of the photocatalytic applications. These limitations can be overcome by adopting various strategies to minimize these phenomena and to improve its photocatalytic efficiency and performance in the visible light region.

In the last few years, heterostructure/heterojunction formation with semiconductors has been recognized as an effective technique to enhance the photocatalytic performance of semiconductors [13–15]. For that, the effect of crystal facets optimization, doping with metal and non-metal surface defects, heterojunctions formation with other semiconducting materials, and, finally, noble-metal-based nanocomposites were investigated as visible-light-driven photocatalysts [7,16,17].

While gold plasmonic nanoparticles used alone can activate the degradation of organic dyes under visible light irradiation, as reported by D. Latha et al. for methylene blue and methyl orange [18], composite systems are mostly composed of metallic nanoparticles of Ag, Au, Pd, and Pt deposited on TiO_2 oxides or on 2D structures such as C_3N_4/Graphene [19–23]. Very few studies have been reported on noble metal/WO_3-based photocatalysts for organic dye pollutant degradation with advanced characterization. The Au/WO_3 system was first developed as a sensitive layer for gas detection and then used as a catalyst [24,25]. A silver-based Ag/WO_3 composite was investigated by Gondal et al.; they reported that the presence of Ag NPs with a strong localized surface plasmon resonance (LSPR) promoted charge carriers' generation and enhanced efficient photogenerated electron–hole pair separation [26].

However, other mechanisms of synergy between metal particles and a semiconductor can also intervene and contribute to the improvement of photocatalytic performances, such as: (i) a local heating effect [22,27–30], (ii) charge transfers between the two materials, and (iii) new sites of adsorption and possible redox reactions for the pollutants or the oxidizing

species (i.e., directly on the gold nanoparticles or at the two-phase interface). Moreover, the formation of a hybrid junction is accompanied by the creation of a Shottky barrier that inhibits the recombination of photoexcited electron–hole pairs [31–33].

In recent work, we studied the photocatalytic properties of an Au composite deposited on WO_3 nanoplatelets, as compared to the oxide alone [34]. Using advanced characterization of the MB decomposition products by LC-MS, we evidenced different degradation pathways for the composite and the bare oxide. As our previous studies showed that the WO_3 morphology itself plays a role in catalytic and photocatalytic performances [34–36], we have developed composite materials based on gold nanoparticles that are grafted directly onto WO_3 templates with various morphologies [37]. In this work, we reported the photocatalytic activities of the synthesized Au/WO_3 nanocomposites under solar light irradiation. In addition to the role of the WO_3 oxide as a support for composites, its photocatalytic efficiency was investigated according to several factors like: (i) synthesis parameters of the composites, template morphology; (ii) reaction medium parameters (type of dyes, pH of the solution, and catalyst loading). The effects of these factors on the dye degradation performance will be discussed. At the end, a photodecomposition mechanism is proposed, based on scavenger tests.

2. Experimental Setup

2.1. Chemicals

The tungsten oxide precursors ($NaWO_4$, $2H_2O$; CAS Nb. 10213-10-2), $(NH_4)_{10}(W_{12}O_{41})\cdot 6H_2O$, gold (III) chloride trihydrate ($HAuCl_4$,$3H_2O$; CAS Nb. 16961-25-4), and sodium borohydride ($NaBH_4$; CAS Nb. 16940-66-2) were purchased from Sigma-Aldrich (Lyon, France). Rhodamine B (CAS Nb. 81-88-9), methylene blue (CAS Nb. 61-73-4), and methyl orange (CAS Nb. 547-58-0) were purchased from ChemLab (Lyon, France). All reagents were used without any further purification. All the synthesis and characterizations using water were carried out with 18 MΩ deionized water.

2.2. Materials Syntheses

WO_3 oxides: the nanoplatelets (NP) and pseudospheres (PS) of WO_3 oxide particles were synthesized with sodium tungsten dihydrate $Na_2WO_4\cdot 2H_2O$ and ammonium tungstate hexahydrate $(NH_4)_{10}(W_{12}O_{41})\cdot 6H_2O$, respectively, as precursors by using a simple free template precipitation method. The WO_3 nanoparticles were synthesized in our laboratory following the same method reported in our previous works [35,36]. The use of these two precursors in aqueous media and in absolute ethanol enables the synthesis of two different morphologies. The obtained yellow precipitate was filtered, washed with distilled water and absolute ethanol several times, and, finally, calcined at 500 °C for 2 h in air.

Au/WO_3 nanocomposites: The synthesis details of Au/WO_3 composite are reported in our previous work [37]. Gold nanoparticles were obtained on the surface of nanostructured tungsten oxide using an impregnation-reduction method at room temperature. First, an amount of previously synthesized WO_3 was dispersed in a gold precursor solution. The mixture was stirred in the darkness for 48 h before adding 0.15 mmol of freshly prepared $NaBH_4$ solution. The reduction took place and led to the nucleation and growth of gold nanoparticles by oxidation state modification from auric ions to metallic state. After the reduction, which was executed in an ice-cooled bath, the composite powder was washed with water/ethanol by centrifugation and dried overnight under airflow at 60 °C in an oven. Considering the ratio between the gold precursor and the WO_3 suspension, the elaboration parameters of the nanocomposite were optimized according to the gold loading rate (1 and 5 wt.%), the $HAuCl_4$ precursor concentration (2.5×10^{-4} to 10^{-2} mol/L), and the impregnation time (24 h to 72 h).

2.3. Characterization Methods

The crystal structure of WO_3 was determined via X-ray diffraction (XRD) (EMPYREAN Panalytical diffractometer, Netherlands) with a Cu Kα source, at a voltage of 45 kV, the current being 35 mA. X-ray patterns were compared with those of the International Centre for Diffraction Datasheet (ICDD). The morphological characterizations of the powder were conducted by Scanning Electron Microscopy (SUPRA 40Vp Colonne Gemini Zeiss SEM, Jena, Germany, operated at 10 kV) and Transmission Electron Microscopy (Tecnai G2, Europe, operating at 200 kV, with a resolution of 0.25 nm). The chemical composition of the synthesized materials was evaluated by energy dispersive spectroscopy (EDS). The EDS results allowed us to compare the experimental composition to nominal synthesis values.

Texture was analyzed using nitrogen sorption at −196 °C. The measurements were done using a BELSORP Max 1 apparatus (Germany). Specific surface area and pore size distribution were deduced from the obtained isotherms. Prior to the measurements, the samples were evacuated at 150 °C under vacuum for 15 h in order to remove any adsorbed species.

The oxidation state of the elements as well as the metal–oxide interaction were monitored using X-ray photoelectron spectroscopy (XPS) measurements. The XPS spectra were acquired with a PHI 5000 Versaprobe apparatus (Europe) with an Al $K_{\alpha 1}$ radiation source (energy = 1486.7 eV, accelerating voltage = 15 kV, power = 50 W, and spot size diameter = 200 µm). Pass energies of 187 eV and 58.7 eV were used for survey spectra and high-resolution windows, respectively. The textural analysis was characterized by gas adsorption. Sorption isotherms were measured at −196 °C using BELSORP Max 1 apparatus. Prior to the measurement, the samples were treated at 150 °C under vacuum for 15 h in order to remove any adsorbed species. Optical absorbance and UV-visible diffuse reflectance spectra (DRS) were collected with a SHIMADZU 2600 UV-Vis/NIR spectrophotometer (Shimadzu Europa). The reflectance (R∞) was recorded with respect to $BaSO_4$ reference, and the band-gap energy was calculated according to the Kubelka–Munk function.

Photodegradation applications: The photocatalytic properties were evaluated on different model pollutants such as dye molecules. Methylene blue (MB) and Rhodamine B (RhB) were chosen as cationic molecules while methyl orange MO was selected as an example of anionic dye. The photocatalytic test device was equipped with an artificial solar light source (Osram Ultra-Vitalux lamp France 300 W, $\lambda > 364$ nm). Considering all device's parameters (the distance between the lamp and the surface of the solution, the power of the lamp, and the dimensions of the used beaker), the irradiance was estimated at 600 $W \cdot m^{-2}$.

In a typical experiment, photocatalytic powder (1 mg/2 mL) was dispersed in a pollutant solution with a concentration of 1×10^{-5} $mol \cdot L^{-1}$. The adsorption–desorption equilibrium between the particles and the pollutant molecules was obtained under a vigorous stirring in the darkness for one hour. Then, the solar light lamp was switched on and the mixture was irradiated. A total of 3 mL of the suspension were collected at regular time periods during irradiation. After removal of the powder, the samples were analyzed by UV-visible spectrophotometry. The evolution of the pollutant concentration was estimated by colorimetric method considering the absorbance at 554, 664, and 464 nm for, respectively, RhB, MB, and MO. The formation of oxidative radicals in the photocatalytic process was investigated using scavenger compounds—isopropanol (IPA), ethylenediamine tetra-acetic acid disodium salt (EDTA), and benzoquinone (BQ)—to trap $^{\bullet}OH$, h^+, and $^{\bullet}O^{2-}$, respectively.

3. Results and Discussion

3.1. Structural and Microstructural Characterization of WO_3 Oxide Templates

The structural analyses were done by X-ray diffraction. Figure 1 shows the XRD patterns of the samples. Both patterns correspond to a well-crystallized tungsten oxide phase. The observed Bragg peaks are characteristic of a single pure phase of WO_3, without additional peaks from residual impurities. At 500 °C, the calcination temperature used, WO_3 can be crystallized in a monoclinic or orthorhombic lattice, with very close lattice

parameters. According to our previous studies based on Rietveld refinements [35,36], both diffractograms were indexed with an orthorhombic phase (ICSD n° 050727) rather than a monoclinic one (ICSD n° 000836), with a *Pmnb* (n° 62) space group. The refinement position gave a set of structural parameters with low deviation, such as a = 7.341 Å, b = 7.570 Å, c = 7.754 Å, and $\alpha = \beta = \delta = 90°$. Depending on the nanopowders morphology, different intensities were be observed for the main peaks at 23.1°, 23.6°, and 24.3° corresponding to (002), (200), and (020) plans, respectively. Compared to the reference profile, the relative peak intensities are roughly in accordance for the PS sample, while they are inverted for the NP sample (especially the two first one). This may be linked to a different morphology of NP particles that favors preferential orientation.

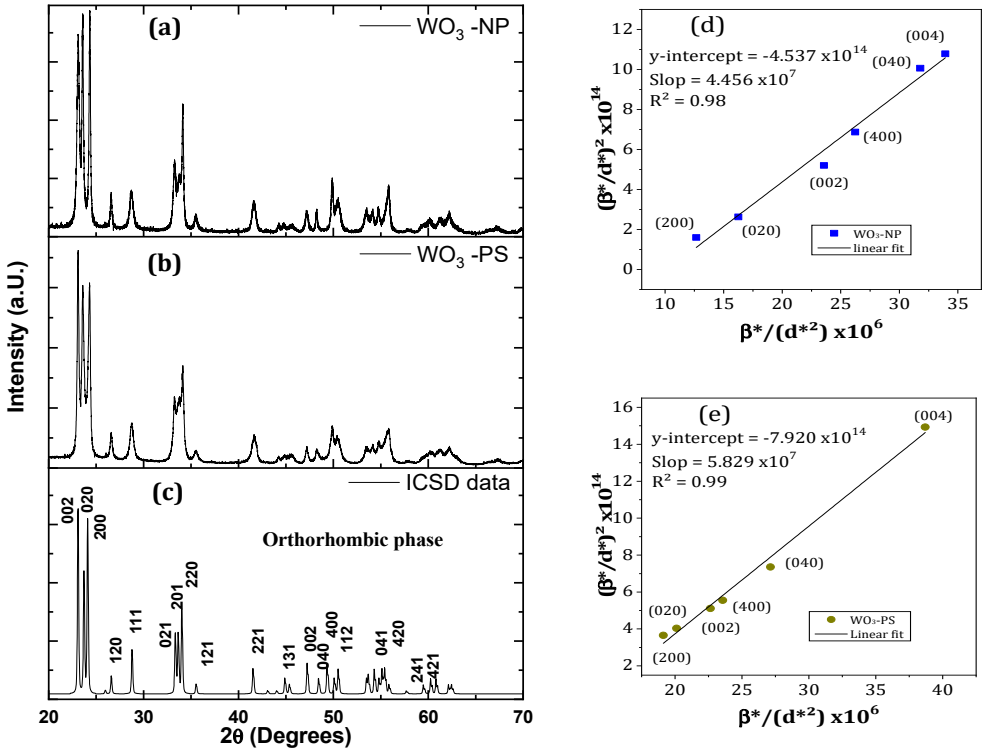

Figure 1. XRD patterns of (**a**) WO_3 nanoplatelets, (**b**) nanospheres, and (**c**) orthorhombic ICSD datasheet; (**d**,**e**) Halder–Wagner plot for the (002), (020), and (200) planes families of (**a**) WO_3 NP and (**b**) WO_3 PS.

To de-correlate the effects of the stress and crystallites size on the peaks broadening, the crystallite sizes were estimated according to the Halder–Wagner (H-W) method. This method differs from the Williamson-Hall method since it gives a greater weight to the contributions of the sample (β^*_{samp}) to the half width at the half maximum (HWHM) value broadening of the X-ray diffraction peaks located at low and medium angles [38]. The equation used is the following:

$$\left(\frac{\beta^*_{samp}}{d^*_{hkl}}\right)^2 = \frac{1}{D} \times \frac{\beta^*_{samp}}{{d^*_{hkl}}^2} + \left(\frac{\varepsilon}{2}\right) \quad (1)$$

With $\beta^*_{samp} = (\beta_{samp} \times cos\theta)/\lambda$ and $d^*_{hkl} = (2 \times d_{hkl} \times sin\theta)/\lambda$, and with θ being the diffraction angle, λ the analysis wavelength, D the crystallite diameter, and ε the strain. Figure 1e,f show the plot of $(\beta^*_{samp}/d^*_{hkl})^2$ versus $(\beta^*_{samp}/{d^*_{hkl}}^2)$ for WO_3-NP and WO_3-PS, considering that the crystallites of both materials are isotropic. The crystallite size is estimated to be 22 nm for WO_3 NP and 17 nm for WO_3 PS.

However, platelet-shaped particles are anisotropic. The calculations of D and ε were thus carried out separately for the three families of planes which constitute the various faces of a nanoplatelet. Considering the broadening and overlapping of the diffraction peaks at high angles which were observed in the WO_3 NP diffractogram, only two peaks per family could be used for the calculations. The results are grouped in Table 1.

Table 1. Crystallite size and deformation of the particles from Halder–Wagner method.

	WO_3-NP				WO_3-PS
	All (hkl)	**(020)**	**(200)**	**{002)**	**All (hkl)**
D (nm)	22	19	21	26	17
$\varepsilon \times 10^6$(u.a.)	42.6	54.1	49.6	36.4	56.3

As will be discussed hereafter, these values are far from the dimensions determined by direct measurement on the microscope images.

Chemical analyses based on XPS characterization were performed to determine the elemental composition and chemical state of the materials. The spectra presented in Figure 2a show the detection of the W and O elements. The presence of sodium (Na) in the spectrum of WO_3 NP can be attributed to a synthesis residue coming from the tungsten precursor and not completely removed during washing step. To ensure that sodium is not present in the crystalline structure, matching tests between the XRD profiles of the samples and those of the ICSD database composed of W, O, and Na were performed via HighScore software. No reference profile was found to match. Moreover, since this element was not detected by other control chemical analyses (EDS type), it was be neglected in the continuation of the study.

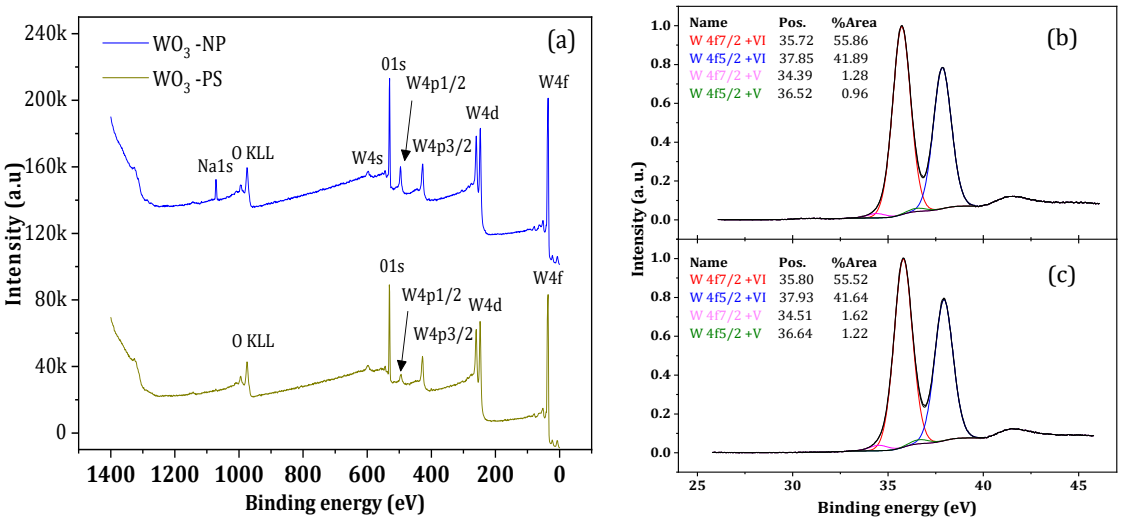

Figure 2. (**a**) XPS spectra of WO_3-NP and W Briggs O_3-PS oxides; (**b**,**c**) high-resolution measurements of W4f levels located between 25 and 45 eV of (**b**) WO_3-NP and (**c**) WO_3-PS.

A detailed analysis, by means of high-resolution measurements, of the spectra corresponding to the 4f level of W evidenced four peaks for both samples (Figure 2b,c). The first two major peaks, located at 35 eV and 37 eV, correspond to the bond energies of W $4f_{7/2}$ and W $4f_{5/2}$, respectively. They are in agreement with the W^{6+} ion energy values reported in the literature [39–41]. The two minor peaks of low intensity indicate the presence of less-oxidized W species such as W^{5+} [42]. In addition, the presence of W^{5+} ions implies the presence of oxygen vacancies [43]. WO_3 has a perovskite-like structure that is mainly formed by edge- and corner-sharing with WO_6 octahedra [35]. Under the calcination, some W-O bonds broke, leading oxygen molecules to leave the surface lattice, which creates

oxygen vacancies [44]. One oxygen vacancy generates two electrons, which reduces W^{6+} ions into W^{5+}, and reduces the number of cations observed by XPS. The 1s oxygen energy levels for WO_3-NP and WO_3-PS, respectively, were observed and have been broken down into three different peaks. The predominant peak, located at a maximum of 530 eV, corresponds to the O^{2-} oxygen ions in the lattice, the peak located at 531 eV corresponds to the HO^- hydroxyl groups [45], and the peak located at 533 eV was caused by the presence of H_2O water molecules [46]. As an indication, the XPS analysis also allowed for the determination of the atomic concentrations of the detected elements. The ratio between the atomic concentration of oxygen and tungsten is equivalent to three, which indicates a material composition in the expected stoichiometric proportions.

Figure 3 shows microscopy images (SEM and TEM) and electron diffraction patterns of the calcined materials issued from the two synthesis routes. The SEM images reveal that WO_3 particles have either the shape of pseudospheres (PS) or NP. After heat treatment at 500 °C, these morphologies are consistent with those that were expected.

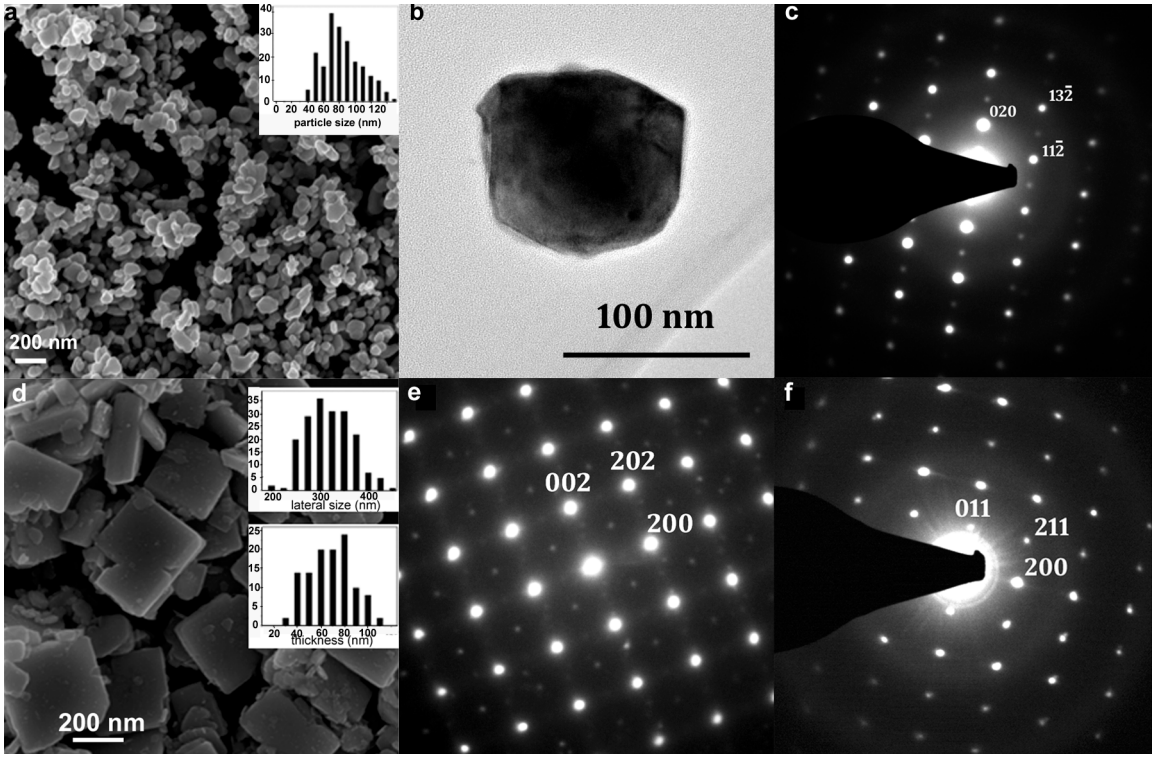

Figure 3. SEM image of WO_3 PS (**a**) and WO_3 NP (**d**), insert histograms correspond to the size distribution. (**b**) TEM image of WO_3-PS and (**c**) its electronic diffraction pattern ([201] zone axis). (**e**,**f**): diffraction patterns of a WO_3 NP along the [010] and the [011] zone axes, respectively.

For PS particles, the average diameter increases significantly (by about one third), with a higher polydispersity from 64 ± 17 nm to 84 ± 31 nm after treatment at 500 °C. At the end of the synthesis, the pseudospheres aggregate by forming clusters of micrometric particles, but this aggregation effect is strongly reduced after treatment at 500 °C; this can be explained by an improvement in the crystallinity and an increase in the surface tensions between the particles.

In the case of the nanoplatelets treated at 500 °C, lateral sizes show a size distribution centered around 300 nm while that of the thickness is around 60–70 nm, i.e., twice as much as before treatment. This is in agreement with the literature, which lists numerous studies on the increase in particle size when heat treatment is applied [47–49]. All NP average dimensions, as estimated by direct SEM measurements, are three to four times higher than those calculated from the Halder–Wagner method. The important difference obtained with the Halder–Wagner method is related to the quality of the diffractograms.

They showed high FWHM (a direct consequence of the small size of the crystallites), as well as a limited number of diffraction peaks that are usable for each family of planes and diffraction lines, and which are mainly located at the mid-angles' region. Although the Halder–Wagner model was precisely chosen in this work for its better consideration of the peaks located at middle angles, compared to other calculation models, it did not allow us to obtain crystallite size values that were consistent with the rest of our analyses.

Moreover, the polydispersity in size of a WO_3 NP sample can influence the FWHM of the diffraction lines and thus distort the crystallite size calculation, as well as the amount of deformation of the nanoplatelets observed in HREM [37], which will be described hereafter.

The observations were fast for the WO_3 PS sample due to the isotropic and non-faceted morphology of the particles. Figure 3c shows an electron diffraction pattern, which is indexed according to an orthorhombic structure of the space group Pnma (n° 62) along the zone axis [201], in agreement with the XRD analyses.

The nanoplatelets can be observed in different orientations (Figure 3d), to obtain the most relevant information, they are studied flat or on the lateral side. The associated electron diffraction patterns are indexed according to the structure of the orthorhombic phase: with a [010] zone axis (Figure 3e) for a platelet observed flat and [001] and [100] zone axes for a platelet seen on the lateral side. Given the dimensions of the particles, [101], [011], and [110] orientations (Figure 3f) are often obtained.

The diffraction pattern presented in Figure 3e shows a quadratic symmetry with intense spots corresponding to the (200) and (002) planes of the WO_3 pseudocubic structure and spots of lower intensities, indexed in the orthorhombic structure, which are induced by the deformation and tilt of the WO_6 octahedra. The diffraction pattern in Figure 3f corresponds to a platelet seen on the lateral side according to the [011] orientation. The electron diffraction images also allowed us to index the planes (020) as being the base planes of the platelets. In a former work, some faults in the stacking of the (0k0) planes were detected, illustrated by the presence of diffuse streaks following the $\boldsymbol{b}^*$ axis in the diffraction patterns. These stacking faults are directly observable on the HREM images. Observation of the platelets, when oriented with the $\boldsymbol{b}$-axis parallel to the electron beam, revealed the presence of pores on the surface of the (020) planes [37].

The nitrogen adsorption-desorption isotherms obtained for WO_3-NP and WO_3-PS particles are given in Figure 4. According to IUPAC classification, they belong to the type IV isotherms which is characteristic of mesoporous materials. The position of the hysteresis for WO_3-NP (at p/p° values close to 1) suggests the presence of large mesopores. The B.E.T. equation was used to calculate the specific surface area. The obtained values are equal to 12 $m^2 \cdot g^{-1}$ and 7 $m^2 \cdot g^{-1}$, respectively, for WO_3-NP and WO_3-PS (results not represented here).

The Barrett, Joyner, and Halenda (B.J.H.) method was applied to the desorption branch of the isotherms to estimate the pore size distribution [50]. The pore size distributions for both samples are given in Figure 4c,d. The results obtained are in good agreement with the interpretations of the nitrogen sorption isotherms: WO_3-NP possesses an average size around 60 nm, while WO_3-PS has a smaller average pore size, centered around 10 nm.

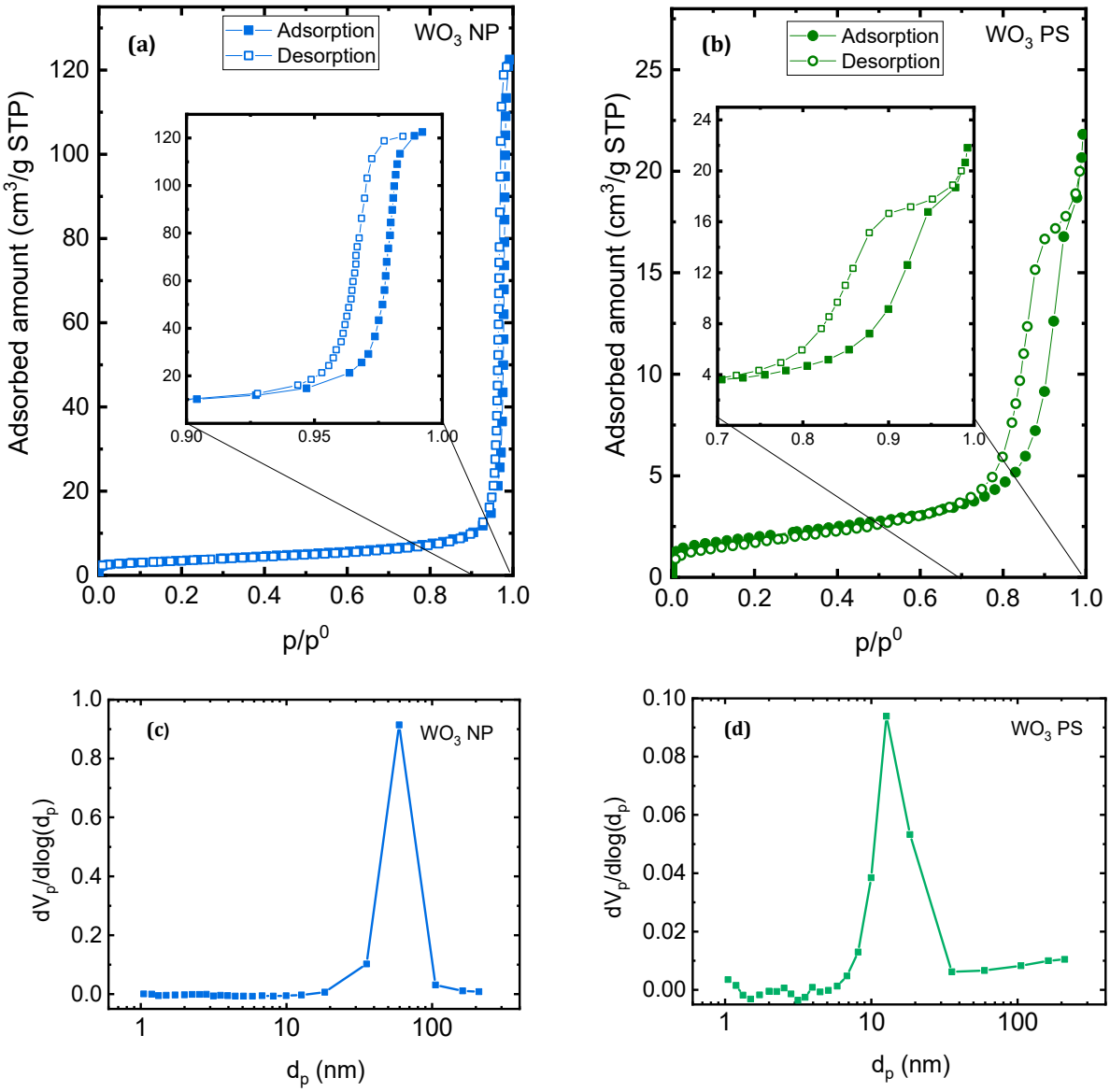

Figure 4. Nitrogen adsorption-desorption isotherms of (**a**) WO_3 NP and (**b**) WO_3 PS, and corresponding pore size distribution calculated using B.J.H. formalism for (**c**) WO_3 NP and (**d**) WO_3 PS.

3.2. Optimization of the Preparation Conditions of Au@WO3 Hybrid Catalysts

The optimization of the elaboration parameters of the composite catalysts was based on the comparison of the photocatalytic efficiencies of the materials obtained in the various tests listed in Table 2. Only the WO_3-NP support, which was expected to be a good support for the deposition of gold nanoparticles, due to its faceted morphology and surface characteristics, was used for these tests. Three parameters were varied: (i) variation in the mass percentage of gold was carried out with the C1 and C2 samples; (ii) $HAuCl_4$ concentration with C2, C3, and C4 samples; and (iii) the impregnation time with C4, C5, and C6 samples. Note that the mass quantity of gold is expressed in a theoretical percentage and was verified by various methods in the subsequent characterizations. The photocatalytic efficiency was studied on the degradation of rhodamine B (RhB) under artificial solar irradiation. The tests were conducted after one hour of stirring in the dark of the Au/WO_3-NP photocatalyst suspended in the polluting solution to establish the sorption equilibrium. Then, the photocatalytic activity was followed by UV-Vis spectroscopy, for 120 min, by recording the decrease in the main absorption band of each dye over the irradiation time.

As an example, Figure 5 shows the evolution of the absorption spectra obtained for each of the polluting dyes in the presence of the Au/WO_3 NP (C5 sample) composite under artificial solar irradiation. As an insert, the histograms represent the relative amount of each dye adsorbed onto the surface of the composite catalyst before the irradiation was started (compared to that onto the bare oxide). These results will be discussed later. For the composite optimization study, RhB dye was chosen for its low adsorption rate and faster photodegradation on the catalyst surface.

Table 2. Synthesis parameters and results of photocatalytic tests for several samples.

Samples	C1	C2	C3	C4	C5	C6
Au (wt.% $_{theo.}$)	1	5	5	5	5	5
$HAuCl_4$ ($mol{\cdot}L^{-1}$)	2.5×10^{-4}	2.5×10^{-4}	10^{-2}	10^{-3}	10^{-3}	10^{-3}
Impregnation time (h)	72	72	72	72	48	24
Relative residual RhB concentration after 120 min of irradiation (%)	49	11	66	56	2	43

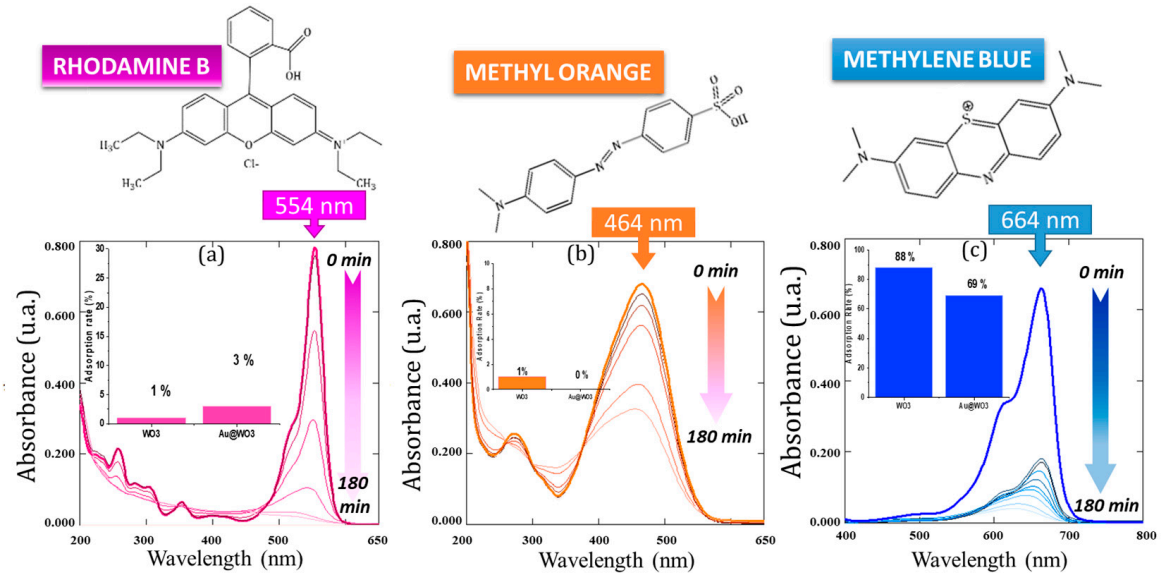

Figure 5. Example of the evolution of the UV absorption spectra of the three dyes tested in the presence of the Au/WO_3 NP C5 photocatalyst during 180 min of sampling: (**a**) rhodamine B, (**b**) methyl orange, (**c**) methylene blue. Insert histograms show the comparison of the adsorption rate of WO_3 vs. Au-WO_3 NP.

3.2.1. Determination of the Optimal Gold Content for the Composite Catalyst

The optimal gold content of the catalyst, in the form of AuNPs grafted onto the oxide surface, is an important parameter. If it is too low, then there may be few gold particles on the surface of the support and the plasmonic, charge transfer, and/or local heating effects engendered by the hybrid particles cannot be obtained. On the other hand, if it is too high, the surface of the support may be overloaded, hindering photon absorption by the semiconductor support, which would slow down the production of (e−/h+) pairs. In the literature, studies focused on the synthesis of Au/WO_3 materials are mainly related to gas sensors [51], methanol conversion [52], H_2O_2-assisted gas photocatalysis, or H_2 production [53]. The gold rates used are very diverse, ranging from 0.1 to 8 wt.%, and generally yield gold particles that are 10 nm in diameter. Because of this, it is not straightforward to determine the amount of gold to load onto WO_3 to improve the photocatalysis results. The first rate of gold loading was determined from the results of Qamar et al. [54]. Their study showed that no improvement in methyl orange (MO) degradation was observed by Au/WO_3 photocatalyst composed of 1 wt.% Au compared to degradation with bare WO_3

support. Therefore, we started with a composite material with this same amount of gold to see if it would be effective on dye degradation. This corresponding sample is named C1. A second gold content of 5 wt.% Au was also studied to observe if a higher amount of Au would improve the properties of the photocatalyst or, on the contrary, degrade them; this sample is named C2.

The results of the photocatalytic tests are presented in Figure 6a and show a degradation efficiency (after 120 min of irradiation of the solution with RhB) of about 90% in the presence of the C2 hybrid against only 50% for the C1 composite. Two conclusions emerge from these results. The first one is that the Au/WO_3 photocatalyst with 1 wt.% of AuNPs degrades only half the amount of RhB present in the medium. Note that the photolysis (without catalyst) or photocatalysis with bare WO_3 reference tests did not show degradation of the solution. The second conclusion is that an amount of 5 wt.% AuNPs leads to a better photocatalytic efficiency. This is probably due to a better distribution of AuNPs on the support, favoring synergistic mechanisms that resulted in a faster kinetic and more intense final degradation rate after 120 min [55]. Therefore, the percentage of gold mass that will be retained for the rest of the study is the one corresponding to the C2 sample, i.e., Au = 5 wt.%.

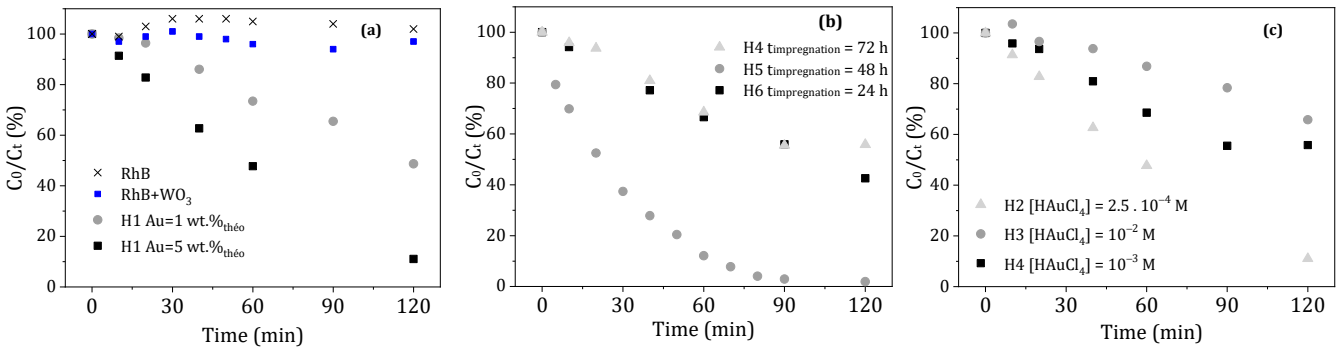

Figure 6. Influence of different composites synthesis parameters on the photodegradation rate and kinetics of RhB: (**a**) gold content of the composite, (**b**) impregnation time of the WO_3 support in the gold precursor solution, and (**c**) concentration of the $HAuCl_4$ gold precursor solution.

3.2.2. Determination of the Impregnation Time

The impregnation time is one of the essential steps for the formation and distribution of AuNPs on the surface of WO_3 support. Three times were studied through the samples C4, C5, and C6, which correspond to an impregnation time of 72, 48, and 24 h, respectively. The results, presented in Figure 6b, do not show significant differences between a 24 and 72 h impregnation time, which both allow a maximum degradation of 50%. However, a clear improvement in the photocatalysis efficiency was obtained with a composite material after 48 h of impregnation, where RhB was 100% degraded in 90 min of irradiation. In order to better understand the influence of the impregnation time on the formation of AuNPs, SEM images were made of these three samples, as seen in Figure 7. For the samples with an impregnation time of 24 and 72 h, the AuNPs that were formed were polydisperse and appeared to be large in size. On the contrary, for the C5 composite obtained after 48 h of impregnation, numerous, very small, and well-dispersed AuNPs were formed on the surface of WO_3 support. The photocatalytic results show that homogeneous coating with small AuNPs on the oxide support is favorable for a better photocatalytic efficiency. The impregnation time of 48 h (corresponding to the C5 sample) was be retained as the best impregnation time and applied for the photocatalytic applications.

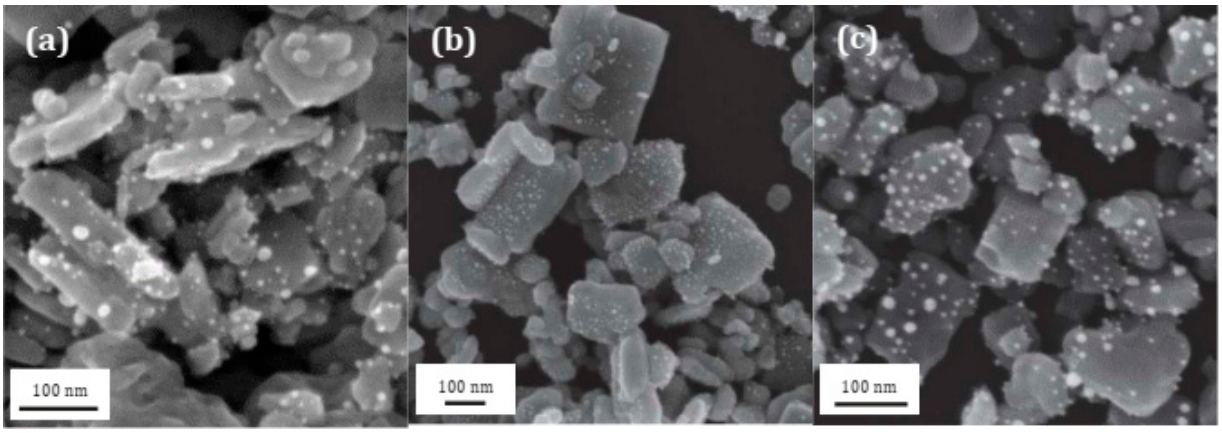

Figure 7. SEM images of (**a**) C4, (**b**) C5, and (**c**) C6 Au/WO_3 NP composites obtained after 72, 48, et 24 h of impregnation in a 10^{-3} M $HAuCl_4$ gold precursor solution, respectively.

3.2.3. Determination of the Optimal $HAuCl_4$ Gold Precursor Solution

To grow and graft the gold nanoparticles on the substrate, tetrachloroauric acid $HAuCl_4$ is used as a precursor. Its concentration seems to be important because it plays a role in the adsorption rate of gold ions on the WO_3 surface. If the concentration is too high, then a strong adsorption of Au^{3+} ions could take place, even in aggregation. In this case, a large number of AuNPs may form on the surface and prevent photon absorption from the WO_3 support or too-large AuNPs may be obtained that are not desirable for a catalytic application. The C2, C3, and C4 samples allowed us to compare $HAuCl_4$ concentrations equivalent to 2.5×10^{-4}, 10^{-2}, and 10^{-3} mol·L^{-1}, respectively, for the same impregnation time of 72 h. According to the evolution of RhB degradation, shown in Figure 6c, the C2 sample obtained with a concentration [$HAuCl_4$] = 2.5×10^{-4} mol·L^{-1} is the most efficient, degrading 90% of RhB in 120 min of irradiation compared to 40% or less for the other two samples. However, if we compare the efficiency of the C2 to the C5 sample presented in the previous paragraph, we notice that the C5 sample has more interesting degradation kinetics and allows for degrading almost all of the RhB molecules in 90 min.

To summarize, the C5 composite material presents the most interesting kinetics and efficiency for RhB degradation. Therefore, the key parameters which we kept for further Au/WO_3 syntheses were the grafting of a gold quantity of 5 wt.% via a 48 h impregnation from a $HAuCl_4$ solution at a concentration of 10^{-3} mol·L^{-1}. These parameters were applied for the next syntheses of composites based on WO_3 NP and on WO_3 PS supports.

Hereafter, advanced characterizations of the composite catalysts are presented. They were elaborated from WO_3 supports treated at 500 °C on which AuNPs were grafted according to the above optimized conditions. The composite materials prepared, respectively, from WO_3-NP platelet-shaped and WO_3-PS pseudospherical particles are named Au/WO_3-NP and Au/WO_3-PS. Two objectives were sought: (i) to confirm the gold content of the elaborated composites, and (ii) to determine the modifications of properties generated by the deposition of AuNPs on the surface of the semiconductor supports (influence on structure, surface, polarity, porosity, band structure, etc.).

3.3. Structural and Microstructural Characterization of Au/WO_3 Composite

The first characterizations to be carried out were to ensure the presence of gold particles and to evaluate the quantity of the grafted particles. On the SEM images (Figure 7), some white particles were observed, which were identified as gold particles by EDS analysis. The EDS spectra presented in Figure 8a,b show, for both materials, the presence of gold with energy peaks detected around 10 and 12 keV and tungsten with an energy peak detected around 8 keV.

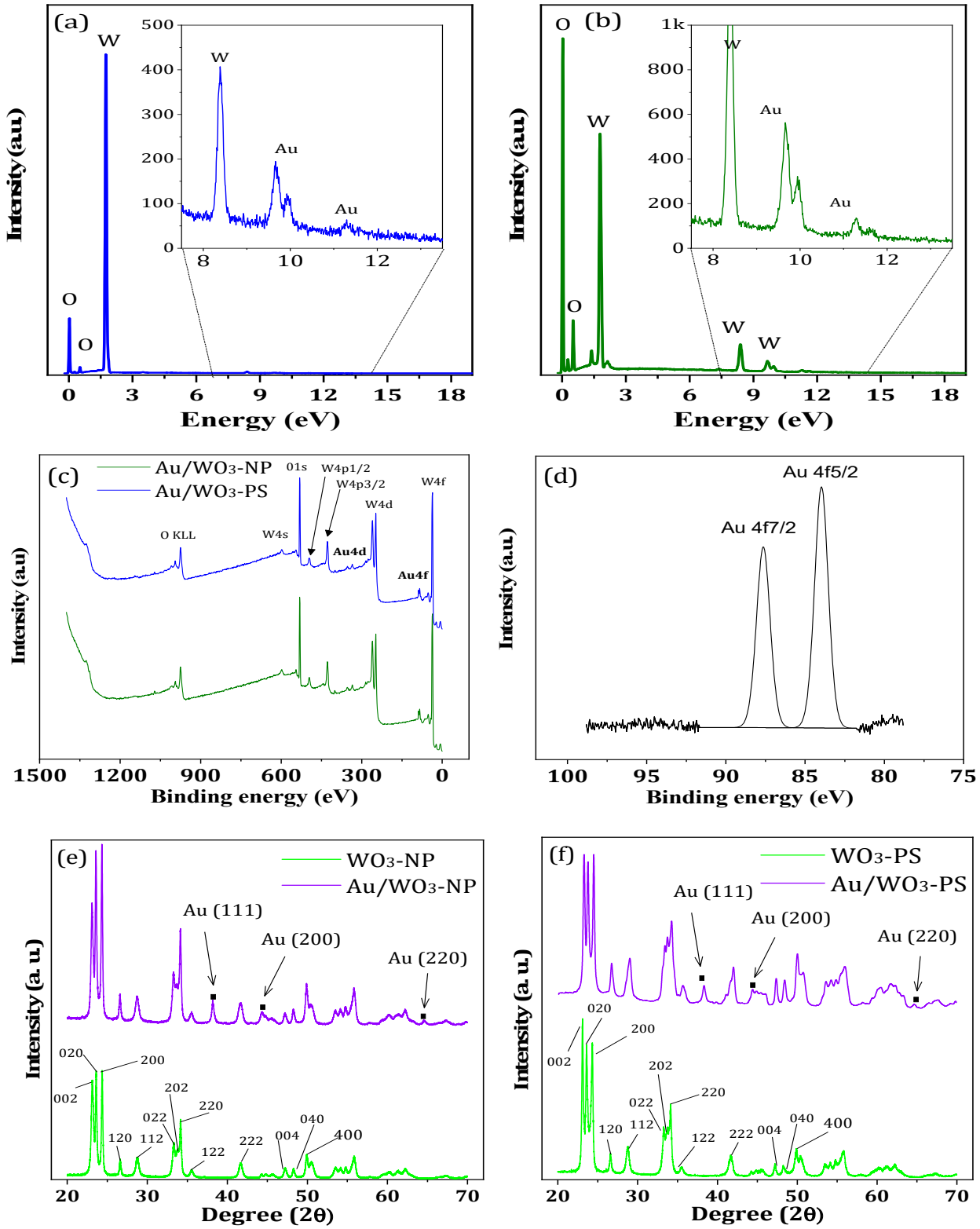

Figure 8. EDS spectra of (**a**) Au/WO_3-NP and (**b**) Au/WO_3-PS nanohybrids; (**c**) XPS spectra of the two hybrids with (**d**) focus on the two energy band located between 75 and 100 eV that are characteristic of metallic gold; XRD patterns of (**e**) Au/WO_3-NP and (**f**) Au/WO_3-PS.

The theoretical mass gold content added to the surface of the oxide supports was 5 wt.%. However, as shown by the results of the mass measurements determined by ICP, the gold rate is lower. It reaches 3.5 wt.% for Au/WO_3-NP and 2.5 wt.% for Au/WO_3-PS. The gold grafting is, therefore, more efficient on the nanoplatelet supports, with a yield of 70% compared to only 50% for the WO_3-PS particles. Moreover, this also shows that good photocatalysis results on RhB were obtained with only 3.5% gold. By optimizing the gold grafting yield on WO_3, it would, therefore, be possible to use less gold precursor to prepare our photocatalysts.

Further investigations on the chemical state between the metal–metal oxide interaction of the composite were collected by XPS analyses. The spectra of the Au/WO_3-NP and Au/WO_3-PS samples are shown in Figure 8c,d. The energy bands corresponding to the W and O elements are identical to those of the bare WO_3 substrates. The Au element is detected at 83.97 and 87.64 eV, values which are in accordance with the $4f_{7/2}$ and $4f_{5/2}$ energy levels of gold in the metallic state (Au^0), respectively [56]. This confirms, for both composite samples, the presence of gold on the one hand and, on the other hand, the good reduction of Au^{3+} ions by $NaBH_4$ to metallic gold.

Figure 8e,f shows the XRD results of the Au/WO_3 samples compared to the bare WO_3 samples given in Figure 1a,b. The diffractograms are very similar except for the presence of three additional peaks for the Au/WO_3 composites. These three peaks, located at 38, 44, and 65°, can be indexed to the (111), (200), and (220) planes of a face-centered cubic structure of gold metal (Fm-3m, space group ICSD No. 52249), respectively. All other diffraction peaks correspond to the orthorhombic phase of WO_3 described in Section 3.1.

SEM images of Au/WO_3-NP (Figure 9a) and Au/WO_3-PS (Figure 9b) composite compounds allowed us to observe the distribution of AuNPs on the oxide supports after grafting. The measurements of the particle size carried out on 1000 AuNPs allowed us to plot the size distribution (inserts in Figure 9a,b). In both cases, the distribution was polydisperse with an average size centered around 7 nm. However, the density of gold particles was higher on the WO_3-NP support than on the WO_3-PS support. In addition, a different distribution between the faces of the WO_3-NP support was observed. The square basal faces have a high density of uniformly distributed gold nanoparticles while the rectangular lateral faces contain very few or no AuNPs. This reflects a selective growth of gold nanoparticles.

TEM observations on WO_3-PS (Figure 9c) and WO_3-NP (Figure 9d,e) confirmed the presence of gold nanoparticles. In the case of nanoplatelets, they are more numerous on the basal side of WO_3 nanoplatelets. Figure 9d corresponds to a platelet observed along the [010] direction, on which the gold nanoparticles appear darker than WO_3; they are seen more clearly when the nanoplatelet is observed on the edge (Figure 9e). For both composites, we notice that the gold particles are more hemispherical than spherical in shape, with a large flat interfacial area between the gold nanoparticle and the WO_3 support (Figure 9e).

The contact zone between the two elements of the composite material is important because it defines the nature of the junction (Schottky or ohmic) and affects the electron transfer between the metal and the semiconductor. For a photocatalysis application, it is preferable to have a large interfacial zone to promote the electronic exchanges between the metal and the semiconductor. In our case, the AuNPs hemispherical shape offers a wide elliptical interface. These configurations allow both the appearance of an additional porosity that is useful during the photodegradation process and an improvement in the electronic properties of the composite materials compared to their bare WO_3 counterparts.

The textural characteristics of the composite were obtained with nitrogen sorption, and adsorption-desorption isotherms are given in Figure 10. The isotherm of WO_3-NP remains type IV after the grafting of the gold particles while that of WO_3-PS changes from a type IV isotherm to a type II isotherm typical of a non-porous or macroporous material. The grafting of AuNPs on the surface of WO_3-PS thus leads to the loss of mesoporosity. The specific surface calculated by the B.E.T. method increases in both cases, after grafting,

from 12 to 16 $m^2 \cdot g^{-1}$ for WO_3-NP and from 7 to 11 $m^2 \cdot g^{-1}$ for WO_3-PS. This increase may be partially linked to the presence of AuNPs. Another hypothesis may be that the grafting procedure of AuNPs (impregnation, reduction, and drying) on WO_3 supports could modify the agglomeration state of WO_3 particles and reduce the intergranular porosity.

The pore size distribution of the Au/WO_3-NPs composites was also estimated using the B.J.H. method (Figure 10b). A decrease in the pore size diameter is observed upon grafting, changing from 60 nm before grafting down to 30 nm after the incorporation of Au nanoparticles. This decrease can be explained by the presence of AuNPs between the platelets of the oxide support. In the case of Au/ WO_3-PS, it is not possible to apply the B.J.H. formalism since the isotherm does not present a saturation plateau.

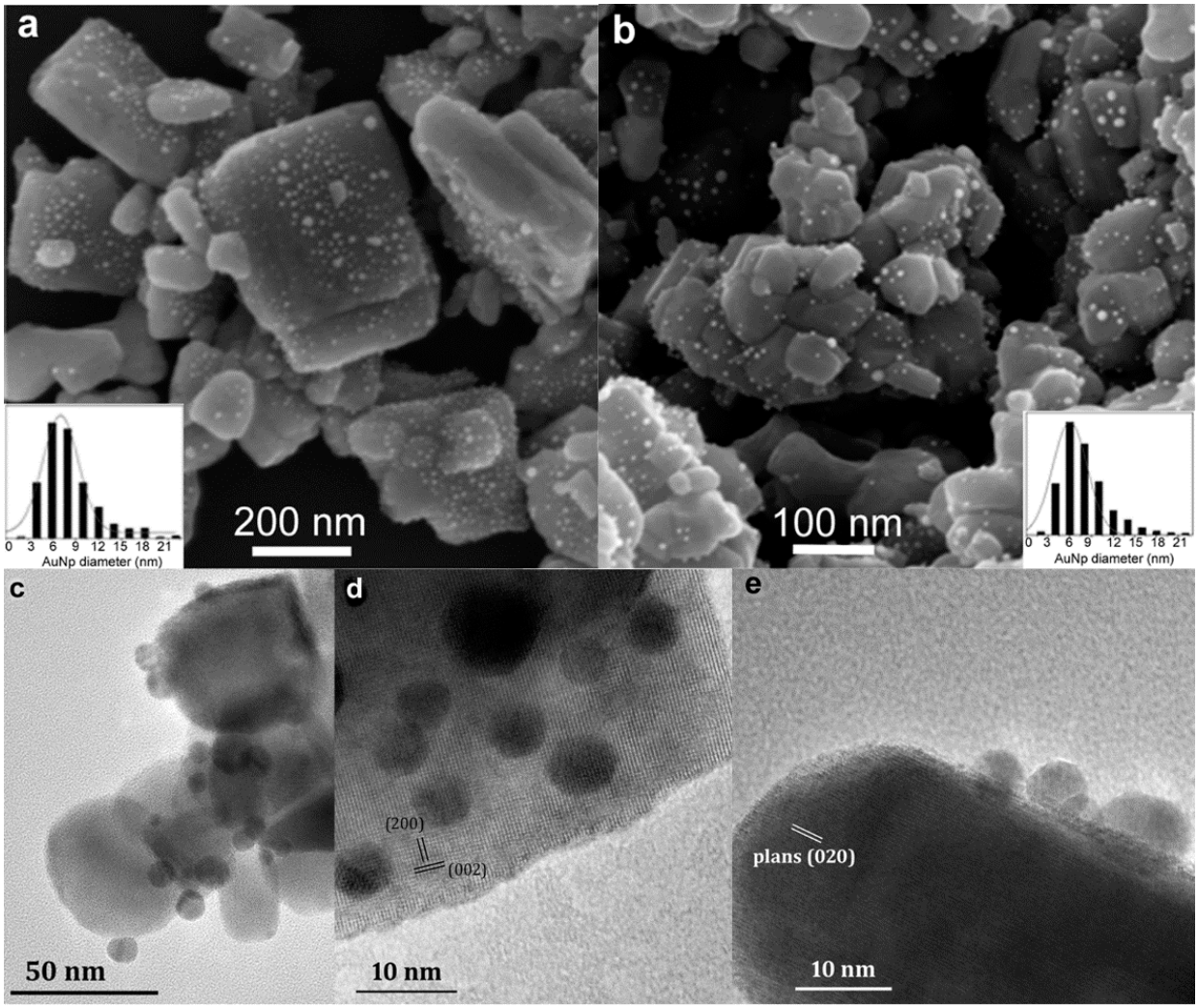

Figure 9. SEM images of (**a**) Au/WO_3 NP and (**b**) Au/WO_3 PS nanohybrids. Inserts show the size distribution of AuNPs diameter as determined by measurements on 1000 NPs. TEM images of (**c**) Au/WO_3 PS and (**d**,**e**) Au/WO_3 NP.

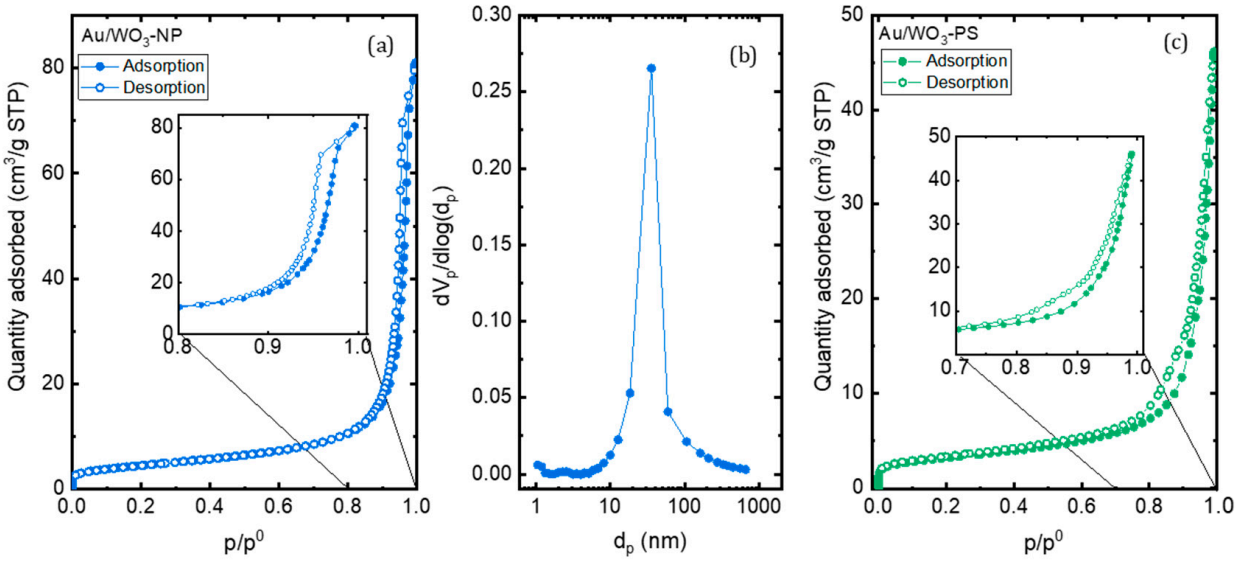

Figure 10. (**a**) Nitrogen adsorption-desorption isotherms of Au/WO_3 NP; (**b**) pore size distribution calculated using B.J.H. formalism; (**c**) nitrogen adsorption-desorption isotherms of Au/WO_3 PS.

3.4. Optical Properties

The photosensitive properties of a semiconductor material depend strongly on its band structure. Many parameters such as morphology, chemical composition, and thermal treatments have an influence on the energy value of the band gap. Figure 11 shows the absorbance spectra in the UV-visible range obtained by DRS analysis. The inserts correspond to the plots of the Kubelka–Munk method, whose extrapolation of the linear part makes it possible to find the bandgap value.

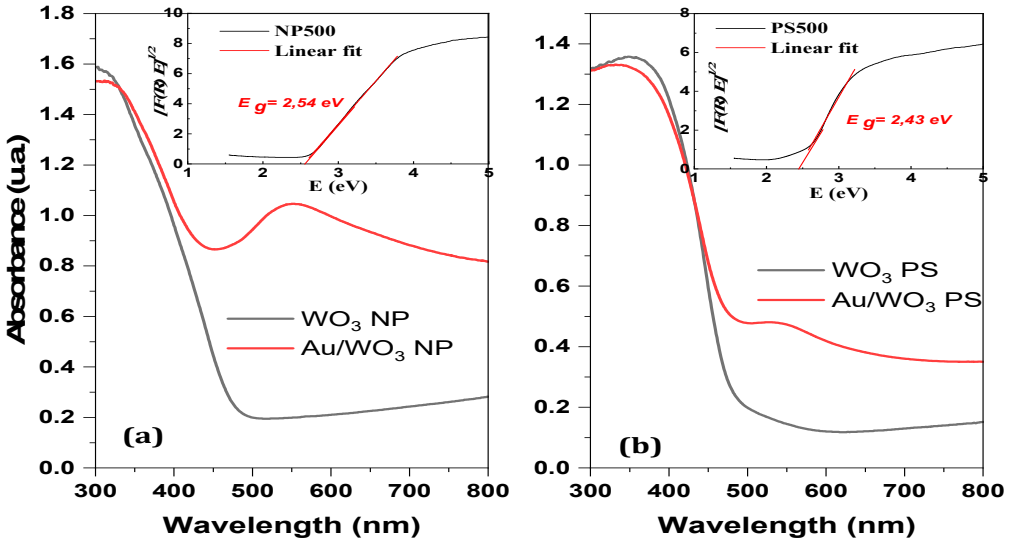

Figure 11. Comparison of DRS measurements in the visible UV range for the materials before (black lines) and after (red lines) gold grafting onto (**a**) WO_3 NP and (**b**) WO_3 PS supports. Insert figures correspond to the Kubelka–Munk plots.

The energies of the conduction ban" (E_{BC}) and the valence band (E_{BV}) are related according to the following equations:

$$E_{BC} = \chi - E^e - 0.5E_g \quad (2)$$

$$E_g = E_{BV} - E_{BC} \quad (3)$$

$$E_{BV} = \chi - E^e + 0.5E_g \quad (4)$$

with E^e being the energy of the free electron at the hydrogen scale equal to 4.5 eV [57], Eg being the band gap energy of the semiconductor calculated by the Kubelka–Munk method, and χ being the geometric mean of the Mulliken electronegativities of the elements in the compound [58].

The estimated gap energies of 2.54 eV for the WO_3-NP supports and 2.49 eV for the WO_3-PS supports are in agreement with the bandgap values of an orthorhombic WO_3 phase that are presented in the literature [59,60]. The wavelengths associated with these bandgap edge values are 488 nm and 498 nm, respectively, indicating that these materials absorb in the visible range.

The absorption spectra of the composite materials compared to those of the bare oxides are shown in Figure 11. The plots representing the composites are composed of two bands. The first is centered around 300–350 nm and corresponds to the bandgap of the WO_3 semiconductor support. The second, centered around 550 nm, corresponds to the surface plasmon resonance (SPR) of the gold nanoparticles [61–63].

It is known from the literature that small gold nanoparticles with diameters less than 5 nm do not have a noticeable SPR effect in DRS [61]. In our case, the measured gold particles have an average diameter of 7($\pm$3) nm for Au/WO_3-NP and 7($\pm$4) nm for Au/WO_3-PS, which explains the low intensity of the absorption peak. In agreement with the results of ICP measurements, it is worth noting that this band is less noticeable for Au/WO_3-PS, which contains less gold, than for Au/WO_3-NP.

3.5. Application to the Photodegradation of Three Dyes (RhB, MO and MB)

As already mentioned, the photocatalytic activity of the catalysts elaborated in this work, bare oxides or composites, was investigated using UV-Vis absorption spectra. Their ability to remove pollutants from aqueous media through adsorption and/or photooxidation were tested with three model molecules and at different pH levels of the aqueous medium (3, 5 as native pH of the dyes solution, and 10). The effect of pH will be discussed in the next section. Here, we focus on the adsorption and photocatalytic properties of the composite catalysts compared to those of the bare oxides at the native pH (i.e., pH = 5) of the dye pollutants solution. Moreover, the differences in the behavior of the catalysts as a function of the morphology of the WO_3 particles, on the one hand, and of the dye which was tested, on the other hand, will be discussed. However, before each photocatalytic application, photolysis tests were carried out to verify the native degradation of pollutants. As reported in Figure 10a, the natural photoactivity over three hours remains low. Except for MB, which degrades to the limit of 25% at the native pH, MO and RhB show degradation rates of less than 5%, whatever the pH of the medium.

The histogram shown in Figure 12 represents a comparison of the adsorption and the photodecomposition rates of polluting molecules on WO_3-based photocatalysts before and after gold grafting, at the native pH. At the end of the adsorption-desorption equilibrium in the dark, the adsorption rate of the MB dye was high for all catalysts, with or without deposited AuNPs, ranging from 50 to 90%. On the contrary, it was very low or negligible for the MO and RhB dyes. These results show a selective adsorption according to the charge and the nature of the organic molecule. With a value of -41 mV at natural pH reported in the literature [63], the zeta potential of WO_3 particles indicates a strong negative surface, thus favoring electrostatic interactions with cationic molecules. In the case of MB, the high adsorption rate is due to the low steric hindrance of the molecules and the high sulfur–oxygen affinity. However, while RhB is also a cationic molecule, it does not have the same affinity with the catalysts surface, onto which it does not adsorb. The RhB steric repulsion of the carboxylate anion could inhibit the adsorption process. For MO, as expected for an anionic molecule, the absence of adsorption is due to the repulsive interactions between MO and the catalysts surface with and without deposited AuNPs. The adsorption difference between the bare oxides WO_3 and the composites Au/WO_3 can be explained by a decrease

in the pores size after gold grafting (from 60 nm to 30 nm and from 50 to 10 nm, for NP and PS shapes, respectively) in which AuNPs are formed, thus decreasing the number of adsorption sites.

At this stage in the treatment with an aqueous environment, our catalyst can be used for the adsorption and recycling of pollutants, like MB dye, with a coacervation process [64]. For the RhB and MO dyes, advanced degradation is more than necessary, given the low adsorption rates.

In addition to the adsorption phenomena, the dye is also removed from the solution by photoinduced oxidation in the presence of the catalyst, this being the so-called photodegradation process. Different photodegradation rates and kinetics are observed depending on the catalyst. As shown by the histogram presented in Figure 12b, the Au/WO_3 composites are clearly more efficient than the bare oxides for the photodegradation of the three studied molecules after 3 h of irradiation, whatever the morphology of the oxide support. This confirms the hypothesis of improved photocatalyst efficiency when there is synergy between the plasmonic particles and the WO_3 semiconductor, which are both photosensitive in the visible range. The degradation rate of MB for both the bare WO_3 NP and PS catalysts reached 65% and 82%, respectively, while the RhB and MO dyes remained undegraded. With both Au/WO_3 catalysts, not only was the photodegradation of MB significantly improved but, also, MO and RhB could be degraded. Thus, the complete decomposition of the RhB was achieved with both composites. For the MB, the photodegradation rate reached 81% and 100% on Au/WO_3NP and Au/WO_3PS, respectively. However, the most appreciated efficiency for both composite catalysts is their ability to degrade methyl orange with degradation rates reaching 48 and 65%, respectively. As reported in the literature, the same type of composite did not show any improvement in MO degradation between a bare WO_3 support and a support loaded with 1 wt.% gold nanoparticles [54].

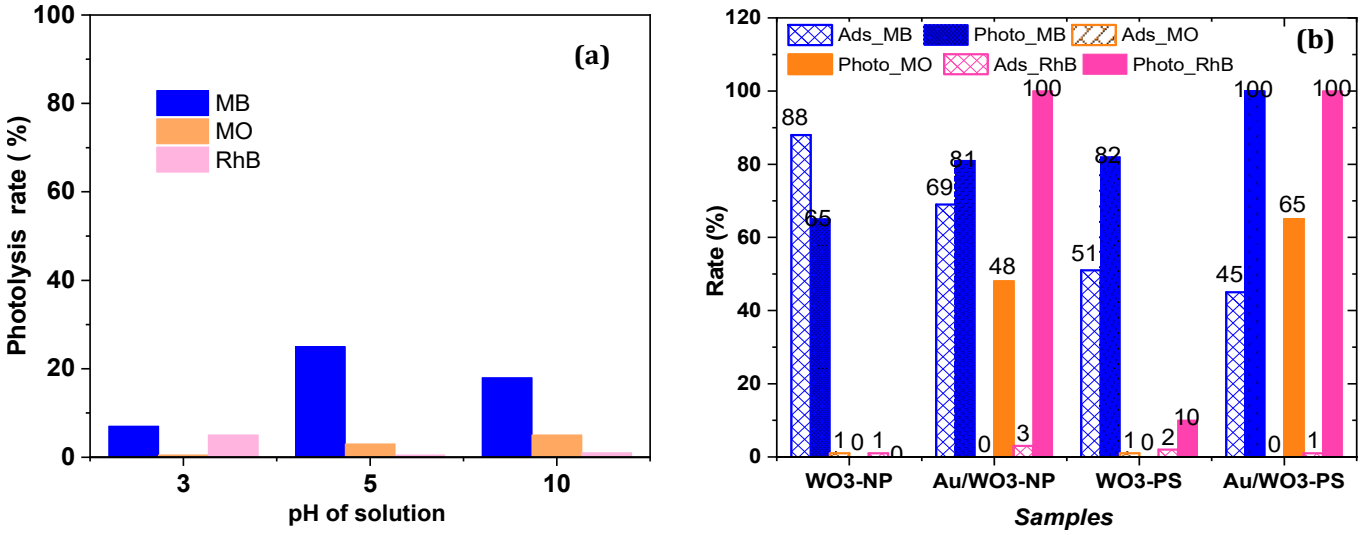

Figure 12. (**a**) Photolysis of the dyes without catalyst. (**b**) Adsorption and photodecomposition rates of the dyes over all catalysts at native pH after 3 h of irradiation.

The photodegradation efficiencies obtained in this work seem very promising. The decomposition rates and kinetics achieved are relatively better compared to works performed under similar conditions. As reported in the literature, the Ag NPs/TiO_2 composites, as the most used plasmonic photocatalyst, allowed researchers to reach a degradation rate higher than 90% during from 60 min to 180 min of irradiation, depending on the polluting dyes [65–68]. D. Ding reported an advanced MO decomposition after 4 h with AuNPs that were 10 nm in size, grafted on TiO_2 oxide [69]. Another composite based on Au NPs loaded on a WO_3/TiO_2 heterostructure was developed for the visible light degradation of phenol and MB [68]. After 120 min of visible irradiation, a 63% decomposition of phenol and a 52%

degradation of MB dye was observed. Qilu Zhang et al. used a similar Au-WO_3 catalyst combined with a carbon structure in a Janus micromotors configuration [70]. It allowed for a fast decomposition of RhB, but the activation movement of the Janus micromotors needed UV light irradiation. Oguzhan Ustun reported only a partial degradation of MB and RhB over WO_3 oxides and Ag NPs/WO_3 even after two hours of irradiation [71]. The reported metal-NPs/oxide catalysts were used for one or two dye pollutants, while our composites (as a versatile catalyst) were shown to be efficient both for cationic and anionic azo dyes.

Figure 13 shows the kinetics of photocatalytic degradation of the three dyes on the Au/WO_3-NP and Au/WO_3-PS composites under solar light irradiation at the native pH of the solutions. We noticed that not only the rate but also the kinetics of the degradation is different for the two cationic molecules, RhB and MB, with the Au/WO_3NP catalyst. To explain this, we must refer to the adsorption rate of the molecule on the photocatalyst, as reported in Figure 12b. Although the deposition of the gold particles on WO_3 decreases the adsorption of MB on the material, it remains important, and inhibits part of the photocatalytic reaction, hence a small improvement of the degradation efficiency of this molecule. With the Au/WO_3PS catalyst, where the MB adsorption rate is significant but not predominant, the kinetics and rate of the RhB and MB dyes degradation are quasi-similar.

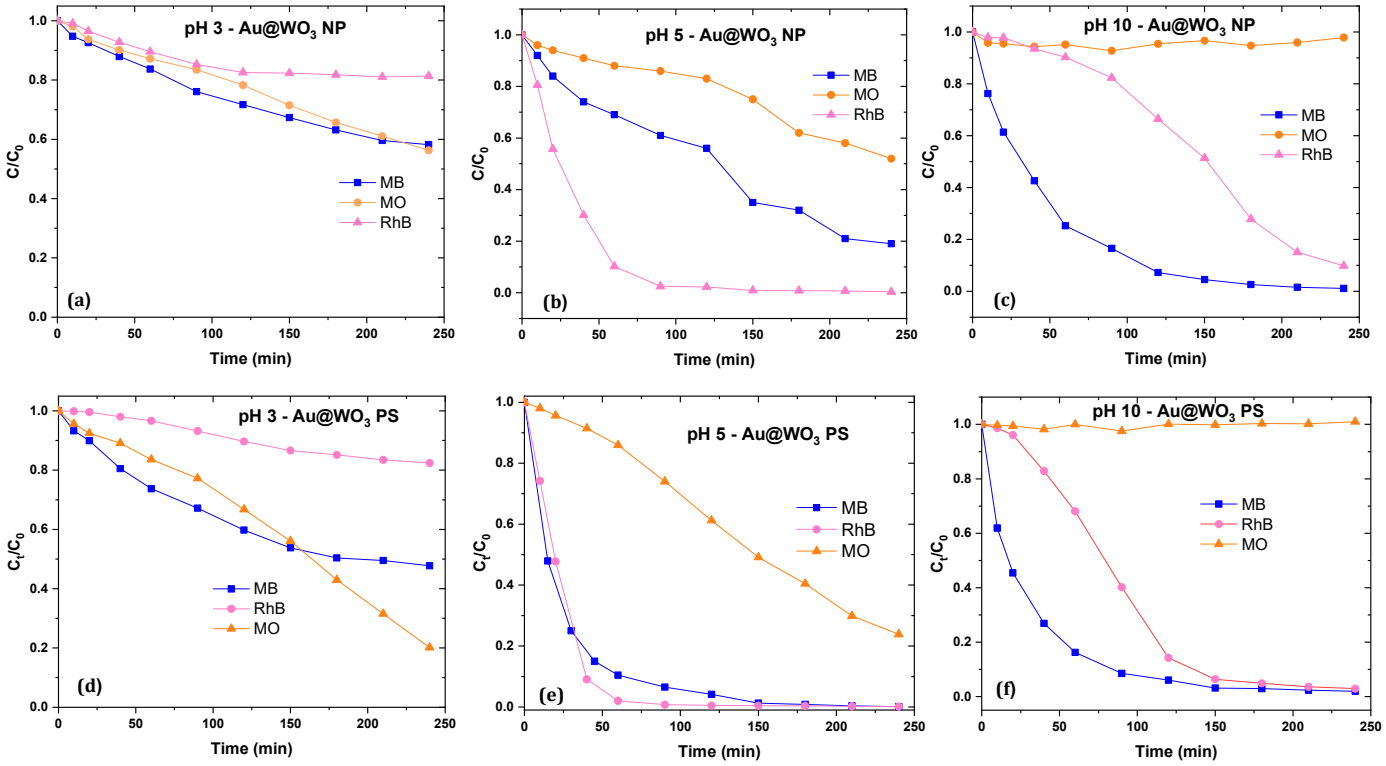

Figure 13. Photocatalytic activities of Au/WO_3 NP and PS: at pH = 3 (**a**,**d**); at native pH of the dyes solutions (pH = 5) (**b**,**e**); at pH = 10 (**c**,**f**).

Moreover, the photocatalytic efficiency is much more important for a cationic molecule. As an example, for RhB, a complete degradation was obtained with the Au/WO_3PS catalyst at a limit of 90 min. In comparison, twice this time (180 min) is required to reduce the initial concentration of an anionic molecule such as MO by half. Photocatalysis being a surface phenomenon, the more the interaction between the polluting molecule and the photocatalyst is reinforced, the more the degradation will be optimal. The degradation rates evolution depends on the charge of the dye molecules and the state of the catalyst surface, such as an attractive interaction which would promote the photocatalytic efficiency while a repulsive interaction which would hinder the degradation process.

According to the obtained photodegradation results, it appears clearly that the oxide supports morphology has a determining role in the photocatalytic efficiency and kinetics of the Au/WO_3 composites. Despite a higher gold content being on the platelets, the degradation kinetics is clearly better with the pseudospherical supports. A microscopic analysis showed different interfaces of the composites: hemispherical contact zones are larger on WO_3 NP than on WO_3 PS. This has a consequence in terms of the energy barrier that the charge carriers have to cross and their lifetime. As reported in our previous work [36], the WO_3 NP-based composite showed a higher photoluminescence than WO_3 PS. Consequently, the lifetime of the charge carriers is higher for PS than for NP, which allows the generation of active radicals, thus promoting a better photocatalytic activity. The photocatalytic results showed an important difference between the two hybrids. The Au/WO_3 PS photocatalyst showed a low adsorption process and an efficient photoinduced activity, giving rise to a complete degradation of RhB and MB, and an advanced decomposition of MO compared to Au/WO_3 NP.

In addition to the stability of the Au/WO_3 catalysts, their recyclability is also important. The results show that, after all cycles, the relative dye concentration that is degraded is equal to 91%, avoiding any possible leaching of metal ions during a photocatalytic test and proving the strong bond between gold and the oxide surface. Overall, we found that composites are significantly more stable than bare oxides [36,37].

3.6. pH Effect on the Photocatalytic Activities of the Dyes (RhB, MO and MB)

The degradation rates evolution depends on the charge of the dye molecules and the state of the catalyst surface, such as the attractive interaction which promotes the photocatalytic efficiency while a repulsive interaction hinders the degradation process. Photocatalytic tests were carried out at different pH levels of the reaction medium: pH 3, native pH 5, and pH 10, as shown in Figure 13. As already mentioned and reported in Figure 12a, photolysis tests were systematically performed, showing a significant degradation for MB (up to 25%), but minor degradation for RhB and MO (less than 5%).

3.7. Photodecomposition Mechanisms

Whatever the composition of the semiconductor photocatalyst, the photodegradation mechanism starts when it absorbs a photon from the irradiation source, which generates electron–hole pairs. Then, the photogenerated holes and electrons may lead to the formation of two main active species, $^{\bullet}HO$ hydroxyl radicals and $^{\bullet}O_2^-$ superoxide anion radicals, with the holes themselves having a strong oxidizing power. These active species are responsible for the degradation of the pollutants and the efficiency of the catalytic system. However, the ability of a semiconductor to generate these radicals depends on the position of the low and high edges of the valence and conduction bands, respectively, in the redox potential scale (referred to NHE). Indeed, $^{\bullet}HO$ hydroxyl radicals come from the oxidation of H_2O molecules by holes, which requires that the low edge of the semiconductor valence band (VB) lies above the oxidation potential of H_2O (i.e., $E(^{\bullet}OH/H_2O) = 2.86$ V vs. NHE); $^{\bullet}O_2^-$ superoxide anion radicals come from the reduction of O_2 molecules by photoinduced electrons, which requires that the high edge of the semiconductor conduction (CB) lies below the reduction potential of O_2 (i.e., $E(O_2/^{\bullet}O_2^-) = -0.33$ V vs. NHE); note that O_2 molecules are generated from water oxidation by holes ($E(O_2/H_2O) = 1.23$ V vs. NHE).

As shown in Figure 14b, holes in the VB of bare WO_3 have a sufficiently high oxidative potential to form $^{\bullet}HO$ hydroxyl radicals and O_2 molecules. However, WO_3 has a CB edge located at +0.5 V vs. NHE, well above the reduction potential of O_2. This means that the photoinduced electrons do not have sufficient potential to generate the $^{\bullet}O_2^-$ radical species on the surface of WO_3, which greatly decreases its photocatalytic efficiency [59]. Only photoinduced holes and $^{\bullet}OH$ radicals can contribute to degrading dye molecules. Besides these oxidative processes, a photobleaching phenomenon, which converts the dye molecules in their colorless leuco or hydrazine derivative forms (reduced forms) may also take place. If so, it contributes to fading the dye solution, without real degradation of the

dye molecules. However, considering the energy level of the conduction band of bare WO_3 PS or NP (E_{CB} = +0.82 eV), this direct reduction would be only possible for RhB molecules ($E_{RhB/LRhB}$ = +0.95 V vs. ENH, $E_{MB/LMB}$ = +0.53 V vs. ENH, $E_{MO/LMO}$ = +0.24 eV [72,73]).

Yet, in the case of our AuNP-based composite catalysts, not only were the yield and degradation kinetics improved, but an efficient decomposition mechanism was observed, which led to molecular fragmentation, as revealed by advanced liquid chromatography assisted with mass spectrometry (LCMS) characterization [29]. As shown in Figure 14, the presence of AuNPs makes it possible to generate $^{\bullet}O_2^-$ superoxide anion radicals using hot electrons.

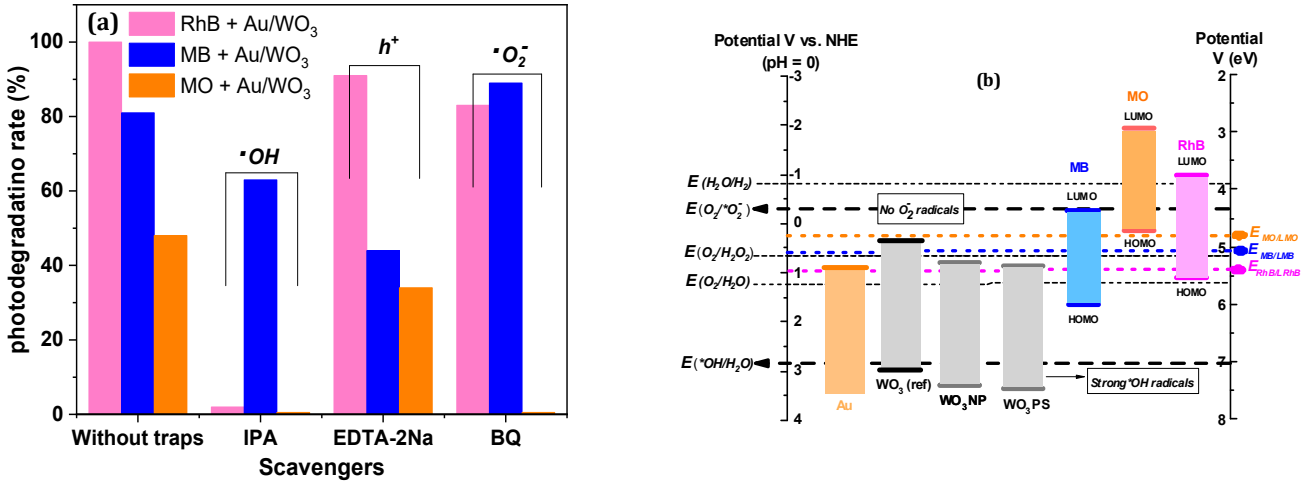

Figure 14. (**a**) Typical studies of radical's identification of Au/WO_3 composites. (**b**) Energy diagram of photocatalysts vs. dyes in relation to the redox potential of active radicals.

Thus, photodegradation on composite catalysts may involve many active species, as illustrated by the following equations:

i. $^{\bullet}HO$ hydroxyl radicals produced by holes at the BV of WO_3 (Equations (6) and (7));
ii. Superoxide anion radicals $^{\bullet}O_2^-$ formed from O_2 generated from water on the surface of gold particles (Equations (4)–(6)). These radicals can also be initiators of other reactive oxidizing species such as $HO_2^{\bullet}$ and $^{\bullet}HO$ (Equations (11)–(13));
iii. The h^+ holes themselves, which can form either in the VB of the semiconductor or within the gold nanoparticle, after excitation. The former can either react with water to form $^{\bullet}HO$ radicals (Equations (6) and (7)) or react directly with the organic molecule on the surface of the photocatalyst (Equation (10)). As for the holes left from the plasmonic excitation of AuNPs, they can form O_2 molecules (Equation (9)).

$$WO_3 + h\nu \longrightarrow h^+_{(WO3)} + e^-_{(WO3)} \quad (5)$$

$$h^+_{(WO3)} + {}^-OH \longrightarrow HO^{\bullet} \quad (6)$$

$$h^+_{(WO3)} + H_2O \longrightarrow HO^{\bullet} + H^+ \quad (7)$$

$$Au + h\nu \longrightarrow \text{hot } (e^-) + \text{hot } (h^+) \quad (8)$$

$$4 \text{ hot } (h^+) + 2H_2O \longrightarrow O_2 + 4H^+ \quad (9)$$

$$O_2 + \text{hot } (e^-) \longrightarrow {}^*O_2^- \quad (10)$$

$$O_2^{\bullet -} + H_2O \longrightarrow HO_2^{\bullet} + {}^-OH \quad (11)$$

$$HO_2^{\bullet} + H_2O \longrightarrow H_2O_2 + HO^{\bullet} \quad (12)$$

$$H_2O_2 + h\nu \longrightarrow 2\,HO^{\bullet} \quad (13)$$

While active species tests performed on Au/WO_3 NP evidenced the majority roles of $^{\bullet}HO^-$ and h^+ in RhB and MB degradation, respectively, for MO dye, all radicals contributed to the degradation process (Figure 14a). The same tests performed with Au/WO_3 PS did not reveal any predominant active species.

The improved photocatalytic performance of WO_3 PS is, therefore, related to the improved charge-carrier creation kinetics due to the new electrical properties provided by the gold particles. This trend is supported by the results reported in the literature. Ab initio (DFT) calculations of electron/hole mobility performed on each of the three facets of the wafers showed a low mobility in the [020] direction compared to the other two directions, [200] and [002] [74]. Therefore, there appears to be a weak charge-carrier transfer between WO_3 (020) and the AuNPs. In the case of WO_3 PS, an isotropic structure, the mobility is an a priori equivalent in the three directions, [020], [200], and [002], thus resulting in a better charge transfer (e−/h+).

As we mentioned before, the gold particle has plasmonic properties that allow it to improve the lifetime of charge carriers by physical effects but also to make thermodynamically favorable redox reactions that were not possible with the position of the E_{VB} and E_{CB} energy levels of bare WO_3. For example, the hot electrons generated by the SPR effect of gold can lead to the formation of O_2 by reaction with water molecules. Once the O_2 species is created, it is possible for it to form secondary oxidizing species such as $^{\bullet}O_2^-$ and HO_2^-, and these species could not be formed by the oxide alone. Thus, the complexity of the reaction mechanism increases with the probability of having many reactive oxidizing species in the presence of the hybrid material, while only $^{\bullet}HO$ is involved in the degradation on bare WO_3. The creation of other active species is favorable for an improvement in the photocatalytic efficiency.

4. Conclusions

In summary, we have discussed the results of dye photodegradation on composite catalysts composed of gold nanoparticles deposited on nanostructured WO_3 oxide supports with various morphologies. These hybrid photocatalysts were synthesized by the impregnation-reduction method. The optimization of the Au/WO_3 composites was carried out by monitoring the photocatalysis of RhB. The optimal synthesis parameters are a 48 h impregnation of five mass percentage of gold from a $HAuCl_4$ precursor with a concentration of 10^{-3} mol·L^{-1}. The confirmation and quantification of gold grafting were obtained by EDS and ICP analyses, and a better grafting yield was observed on WO_3 NP than on WO_3 PS. The XRD analyses did not reveal any modification of the structure of the oxide supports after gold grafting, contrary to the sorption analyses, which highlighted a change in the state of the materials surface, in terms of specific area and porosity. XPS analysis revealed the reduction of W^{6+} ions into W^{5+}. Thus, the appearance of oxygen vacancies favors the composites photocatalysis process with more electron exchanges.

The improvement in the electrical/optical and textural properties of the composite materials was demonstrated, respectively, by the determination of the plasmonic effect of gold on WO_3 supports through DRS measurements and nitrogen sorption.

The photocatalysis results of several dyes pollutants have shown a selective degradation efficiency depending on the charge of the polluting molecules, pH medium, and mass loading of the catalysts. At pH 5 (native), the photocatalysis process is highly efficient on a cationic molecule, and inversely charged with respect to the WO_3 surface, which does not have a strong adsorption capacity. The Au/WO_3 PS composite remains the most efficient, degrading almost the whole RhB and MB in only 60 min and 90 min, respectively. For MO, as anionic dye, the degradation is more efficient in acidic medium (80%) than in basic medium (0%). Trap tests of the main active species involved in photocatalytic degradation

showed a disparity between the two composite materials on the degradation of the same pollutant.

Each of the active species would contribute to the degradation by photocatalysis in the presence of Au/WO_3 PS, while the degradation in the presence of Au/WO_3 NP would be mainly favored by HO^- radicals. To understand the photocatalytic process, further investigations are in progress, both to better identify the charge carriers and their lifetimes by time-resolved spectroscopy but also to identify the decomposition mechanisms by chromatography coupled to the mass spectrometer.

Author Contributions: M.D.: Data curation; Formal analysis; Writing—original draft. M.A. and V.C.: Conceptualization; Writing the draft, Data curation; Formal analysis; Project administration. V.M., M.-V.C., O.H. and H.A.A.: Investigation, Writing—Review & Editing. All authors have read and agreed to the published version of the manuscript.

Funding: This research received no external funding.

Acknowledgments: The authors gratefully acknowledge the Regional Council of Provence-Alpes-Cote d'Azur, Departmental Council of Var (CD83), the urban community of Toulon Provence Mediterranean and University of Toulon for their financial supports in the framework of the "NanoCat", "SemPom" and "Disolar" projects.

Conflicts of Interest: The author declares that he has no known competing financial interest or personal relationships that could have appeared to influence the work reported in this paper.

References

1. Dutta, V.; Sharma, S.; Raizada, P.; Thakur, V.K.; Khan, A.A.P.; Saini, V.; Asiri, A.M.; Singh, P. An overview on WO_3 based photocatalyst for environmental remediation. *J. Environ. Chem. Eng.* **2021**, *9*, 105018. [CrossRef]
2. Din, M.I.; Khalid, R.; Najeeb, J.; Hussain, Z. Fundamentals and photocatalysis of methylene blue dye using various nanocatalytic assemblies—A critical review. *J. Clean. Prod.* **2021**, *298*, 126567. [CrossRef]
3. Dihom, H.R.; Al-Shaibani, M.M.; Mohamed, R.M.S.R.; Al-Gheethi, A.A.; Sharma, A.; Bin Khamidun, M.H. Photocatalytic degradation of disperse azo dyes in textile wastewater using green zinc oxide nanoparticles synthesized in plant extract: A critical review. *J. Water Process. Eng.* **2022**, *47*, 102705. [CrossRef]
4. Vinu, R.; Madras, G. Kinetics of Sonophotocatalytic Degradation of Anionic Dyes with Nano-TiO_2. *Environ. Sci. Technol.* **2008**, *43*, 473–479. [CrossRef]
5. Anwer, H.; Mahmood, A.; Lee, J.; Kim, K.-H.; Park, J.-W.; Yip, A.C.K. Photocatalysts for degradation of dyes in industrial effluents: Opportunities and challenges. *Nano Res.* **2019**, *12*, 955–972. [CrossRef]
6. Matsunami, D.; Yamanaka, K.; Mizoguchi, T.; Kojima, K. Comparison of photodegradation of methylene blue using various TiO_2 films and WO_3 powders under ultraviolet and visible-light irradiation. *J. Photochem. Photobiol. A Chem.* **2018**, *369*, 106–114. [CrossRef]
7. Tang, H.; Tang, Z.; Bright, J.; Liu, B.; Wang, X.; Meng, G.; Wu, N. Visible-Light Localized Surface Plasmon Resonance of WO_{3-x} Nanosheets and Its Photocatalysis Driven by Plasmonic Hot Carriers. *ACS Sustain. Chem. Eng.* **2021**, *9*, 1500–1506. [CrossRef]
8. Shandilya, P.; Sambyal, S.; Sharma, R.; Mandyal, P.; Fang, B. Properties, optimized morphologies, and advanced strategies for photocatalytic applications of WO_3 based photocatalysts. *J. Hazard. Mater.* **2022**, *428*, 128218. [CrossRef]
9. Arab, M.; Madigou, V.; Chevallier, V.; Turquat, C.; Leroux, C. Investigation of Elastic Properties of WO_3 Thin Films Supported on Quartz in Surface Acoustic Wave Sensing Devices. *Electron. Mater.* **2022**, *3*, 124–135. [CrossRef]
10. Acedo-Mendoza, A.; Infantes-Molina, A.; Vargas-Hernández, D.; Chávez-Sánchez, C.; Rodríguez-Castellón, E.; Tánori-Córdova, J. Photodegradation of methylene blue and methyl orange with CuO supported on ZnO photocatalysts: The effect of copper loading and reaction temperature. *Mater. Sci. Semicond. Process.* **2020**, *119*, 105257. [CrossRef]
11. Hunge, Y.M. Sunlight assisted photoelectrocatalytic degradation of benzoic acid using stratified WO_3/TiO_2 thin films. *Ceram. Int.* **2017**, *43*, 10089–10096. [CrossRef]
12. Weng, B.; Wu, J.; Zhang, N.; Xu, Y.-J. Observing the Role of Graphene in Boosting the Two-Electron Reduction of Oxygen in Graphene–WO_3 Nanorod Photocatalysts. *Langmuir* **2014**, *30*, 5574–5584. [CrossRef] [PubMed]
13. Liu, C.; Lü, H.; Yu, C.; Ding, B.; Ye, R.; Ji, Y.; Dai, B.; Liu, W. Novel $FeWO_4/WO_3$ nanoplate with p–n heterostructure and its enhanced mechanism for organic pollutants removal under visible-light illumination. *J. Environ. Chem. Eng.* **2020**, *8*, 104044. [CrossRef]
14. Masuda, T.; Yao, H. Intense Plasmon-Induced Magneto-Optical Activity in Substoichiometric Tungsten Oxide (WO_{3-x}) Nanowires/Nanorods. *J. Phys. Chem. C* **2020**, *124*, 15460–15467. [CrossRef]
15. Wang, L.; Huang, T.; Yang, G.; Lu, C.; Dong, F.; Li, Y.; Guan, W. The precursor-guided hydrothermal synthesis of $CuBi_2O_4/WO_3$ heterostructure with enhanced photoactivity under simulated solar light irradiation and mechanism insight. *J. Hazard. Mater.* **2020**, *381*, 120956. [CrossRef] [PubMed]

16. Manthiram, K.; Alivisatos, A.P. Tunable Localized Surface Plasmon Resonances in Tungsten Oxide Nanocrystals. *J. Am. Chem. Soc.* **2012**, *134*, 3995–3998. [CrossRef] [PubMed]
17. Yan, J.; Wang, T.; Wu, G.; Dai, W.; Guan, N.; Li, L.; Gong, J. Tungsten Oxide Single Crystal Nanosheets for Enhanced Multichannel Solar Light Harvesting. *Adv. Mater.* **2015**, *27*, 1580–1586. [CrossRef]
18. Latha, D.; Prabu, P.; Gnanamoorthy, G.; Munusamy, S.; Sampurnam, S.; Arulvasu, C.; Narayanan, V. Size-dependent catalytic property of gold nanoparticle mediated by Justicia adhatoda leaf extract. *SN Appl. Sci.* **2018**, *1*, 134. [CrossRef]
19. Leong, K.H.; Aziz, A.A.; Sim, L.C.; Saravanan, P.; Jang, M.; Bahnemann, D. Mechanistic insights into plasmonic photocatalysts in utilizing visible light. *Beilstein J. Nanotechnol.* **2018**, *9*, 628–648. [CrossRef]
20. Tanaka, A.; Hashimoto, K.; Kominami, H. Visible-Light-Induced Hydrogen and Oxygen Formation over $Pt/Au/WO_3$ Photocatalyst Utilizing Two Types of Photoabsorption Due to Surface Plasmon Resonance and Band-Gap Excitation. *J. Am. Chem. Soc.* **2014**, *136*, 586–589. [CrossRef]
21. Ren, Y.; Feng, D.; Feng, C.; Dong, X.; Chen, Z. Plasmonic Au/WO_{3-x} heterostructures for enhanced photothermal and photocatalytic performance. *Mater. Today Commun.* **2022**, *31*, 103631. [CrossRef]
22. Wang, Y.; Wang, Y.; Zhao, J.; Chen, M.; Huang, X.; Xu, Y. Efficient production of H_2O_2 on Au/WO_3 under visible light and the influencing factors. *Appl. Catal. B Environ.* **2020**, *284*, 119691. [CrossRef]
23. Adnan, R.; Jalil, A. Gold photocatalysis in sustainable hydrogen peroxide generation. *Mater. Today Chem.* **2023**, *27*. [CrossRef]
24. Yang, X.; Salles, V.; Kaneti, Y.V.; Liu, M.; Maillard, M.; Journet, C.; Jiang, X.; Brioude, A. Fabrication of highly sensitive gas sensor based on Au functionalized WO_3 composite nanofibers by electrospinning. *Sensors Actuators B Chem.* **2015**, *220*, 1112–1119. [CrossRef]
25. Zhang, H.; Wang, Y.; Zhu, X.; Li, Y.; Cai, W. Bilayer Au nanoparticle-decorated WO_3 porous thin films: On-chip fabrication and enhanced NO_2 gas sensing performances with high selectivity. *Sensors Actuators B Chem.* **2019**, *280*, 192–200. [CrossRef]
26. Gondal, M.; Suliman, M.; Dastageer, M.; Chuah, G.-K.; Basheer, C.; Yang, D.; Suwaiyan, A. Visible light photocatalytic degradation of herbicide (Atrazine) using surface plasmon resonance induced in mesoporous $Ag\text{-}WO_3/SBA\text{-}15$ composite. *J. Mol. Catal. A Chem.* **2016**, *425*, 208–216. [CrossRef]
27. Sun, S.; Wang, W.; Zhang, L.; Shang, M.; Wang, L. Ag@C core/shell nanocomposite as a highly efficient plasmonic photocatalyst. *Catal. Commun.* **2009**, *11*, 290–293. [CrossRef]
28. Adleman, J.R.; Boyd, D.A.; Goodwin, D.G.; Psaltis, D. Heterogenous Catalysis Mediated by Plasmon Heating. *Nano Lett.* **2009**, *9*, 4417–4423. [CrossRef]
29. Wu, Z.-C.; Zhang, Y.; Tao, T.-X.; Zhang, L.; Fong, H. Silver nanoparticles on amidoxime fibers for photo-catalytic degradation of organic dyes in waste water. *Appl. Surf. Sci.* **2010**, *257*, 1092–1097. [CrossRef]
30. Yu, H.; Chen, M.; Rice, P.M.; Wang, S.X.; White, R.L.; Sun, S. Dumbbell-like Bifunctional $Au-Fe_3O_4$ Nanoparticles. *Nano Lett.* **2005**, *5*, 379–382. [CrossRef]
31. Khan, M.R.; Chuan, T.W.; Yousuf, A.; Chowdhury, M.N.K.; Cheng, C.K. Schottky barrier and surface plasmonic resonance phenomena towards the photocatalytic reaction: Study of their mechanisms to enhance photocatalytic activity. *Catal. Sci. Technol.* **2015**, *5*, 2522–2531. [CrossRef]
32. He, W.; Kim, H.-K.; Wamer, W.G.; Melka, D.; Callahan, J.H.; Yin, J.-J. Photogenerated Charge Carriers and Reactive Oxygen Species in ZnO/Au Hybrid Nanostructures with Enhanced Photocatalytic and Antibacterial Activity. *J. Am. Chem. Soc.* **2013**, *136*, 750–757. [CrossRef] [PubMed]
33. Tian, J.; Zhao, Z.; Kumar, A.; Boughton, R.I.; Liu, H. Recent progress in design, synthesis, and applications of one-dimensional TiO_2 nanostructured surface heterostructures: A review. *Chem. Soc. Rev.* **2014**, *43*, 6920–6937. [CrossRef] [PubMed]
34. Dirany, N.; Arab, M.; Leroux, C.; Villain, S.; Madigou, V.; Gavarri, J. Effect of WO_3 Nanoparticles Morphology on the Catalytic Properties. *Mater. Today Proc.* **2016**, *3*, 230–234. [CrossRef]
35. Dirany, N.; Arab, M.; Madigou, V.; Leroux, C.; Gavarri, J.R. A facile one step route to synthesize WO_3 nanoplatelets for CO oxidation and photodegradation of RhB: Microstructural, optical and electrical studies. *RSC Adv.* **2016**, *6*, 69615–69626. [CrossRef]
36. Desseigne, M.; Dirany, N.; Chevallier, V.; Arab, M. Shape dependence of photosensitive properties of WO_3 oxide for photocatalysis under solar light irradiation. *Appl. Surf. Sci.* **2019**, *483*, 313–323. [CrossRef]
37. Desseigne, M.; Madigou, V.; Coulet, M.-V.; Heintz, O.; Chevallier, V.; Arab, M. Au/WO_3 nanocomposite based photocatalyst for enhanced solar photocatalytic activity. *J. Photochem. Photobiol. A Chem.* **2023**, *437*, 114427. [CrossRef]
38. Nath, D.; Singh, F.; Das, R. X-ray diffraction analysis by Williamson-Hall, Halder-Wagner and size-strain plot methods of CdSe nanoparticles- a comparative study. *Mater. Chem. Phys.* **2019**, *239*, 122021. [CrossRef]
39. Katrib, A.; Hemming, F.; Wehrer, P.; Hilaire, L.; Maire, G. The multi-surface structure and catalytic properties of partially reduced WO_3, WO_2 and WC + O_2 or W + O_2 as characterized by XPS. *J. Electron Spectrosc. Relat. Phenom.* **1995**, *76*, 195–200. [CrossRef]
40. Li, X.; Lunkenbein, T.; Kröhnert, J.; Pfeifer, V.; Girgsdies, F.; Rosowski, F.; Schlögl, R.; Trunschke, A. Hydrothermal synthesis of bi-functional nanostructured manganese tungstate catalysts for selective oxidation. *Faraday Discuss.* **2015**, *188*, 99–113. [CrossRef]
41. Rong, R.; Wang, L. Synthesis of hierarchical hollow nest-like WO_3 micro/nanostructures with enhanced visible light-driven photocatalytic activity. *J. Alloy. Compd.* **2020**, *850*, 156742. [CrossRef]
42. Shpak, A.; Korduban, A.; Medvedskij, M.; Kandyba, V. XPS studies of active elements surface of gas sensors based on WO_{3-x} nanoparticles. *J. Electron Spectrosc. Relat. Phenom.* **2007**, *156–158*, 172–175. [CrossRef]

43. Soltani, T.; Tayyebi, A.; Hong, H.; Mirfasih, M.H.; Lee, B.-K. A novel growth control of nanoplates WO_3 photoanodes with dual oxygen and tungsten vacancies for efficient photoelectrochemical water splitting performance. *Sol. Energy Mater. Sol. Cells* **2018**, *191*, 39–49. [CrossRef]
44. Higgins, M.C.M.; Hall, H.; Rojas, J.V. The effect of X-ray induced oxygen defects on the photocatalytic properties of titanium dioxide nanoparticles. *J. Photochem. Photobiol. A Chem.* **2021**, *409*, 113138. [CrossRef]
45. Dupin, J.-C.; Gonbeau, D.; Vinatier, P.; Levasseur, A. Systematic XPS studies of metal oxides, hydroxides and peroxides. *Phys. Chem. Chem. Phys.* **2000**, *2*, 1319–1324. [CrossRef]
46. Wagner, C.D. *Handbook of X-ray Photoelectron Spectroscopy: A Reference Book of Standard Data for Use in X-ray Photoelectron Spectroscopy*; Perkin-Elmer Co.: Waltham, MA, USA, 1979.
47. Thilagavathi, T.; Venugopal, D.; Marnadu, R.; Chandrasekaran, J.; Alshahrani, T.; Shkir, M. An Investigation on Microstructural, Morphological, Optical, Photoluminescence and Photocatalytic Activity of WO_3 for Photocatalysis Applications: An Effect of Annealing. *J. Inorg. Organomet. Polym. Mater.* **2020**, *31*, 1217–1230. [CrossRef]
48. Wenderich, K.; Noack, J.; Kärgel, A.; Trunschke, A.; Mul, G. Effect of Temperature and pH on Phase Transformations in Citric Acid Mediated Hydrothermal Growth of Tungsten Oxide. *Eur. J. Inorg. Chem.* **2018**, *2018*, 917–923. [CrossRef]
49. Yin, X.-T.; Lv, P.; Li, J.; Jafari, A.; Wu, F.-Y.; Wang, Q.; Dastan, D.; Shi, Z.; Yu, S.; Garmestani, H. Nanostructured tungsten trioxide prepared at various growth temperatures for sensing applications. *J. Alloy. Compd.* **2020**, *825*, 154105. [CrossRef]
50. Barrett, E.P.; Joyner, L.G.; Halenda, P.P. The Determination of Pore Volume and Area Distributions in Porous Substances. I. Computations from Nitrogen Isotherms. *J. Am. Chem. Soc.* **1951**, *73*, 373–380. [CrossRef]
51. Zhang, B.; Wang, H.; Ye, H.; Xu, B.; Zhao, F.; Zeng, B. Reversible redox mechanism based synthesis of plasmonic WO_3/Au photocatalyst for selective and sensitive detection of ultra-micro Hg_{2+}. *Sensors Actuators B Chem.* **2018**, *273*, 1435–1441. [CrossRef]
52. Wu, X.Y.; Tang, Z.; Zhao, X.; Luo, X.; Pennycook, S.J.; Wang, S.L. Visible-light driven room-temperature coupling of methane to ethane by atomically dispersed Au on WO_3. *J. Energy Chem.* **2021**, *61*, 195–202. [CrossRef]
53. Durán-Álvarez, J.; Del Angel, R.; Ramírez-Ortega, D.; Guerrero-Araque, D.; Zanella, R. An alternative method for the synthesis of functional Au/WO_3 materials and their use in the photocatalytic production of hydrogen. *Catal. Today* **2018**, *341*, 49–58. [CrossRef]
54. Qamar, M.; Yamani, Z.; Gondal, M.; Alhooshani, K. Synthesis and comparative photocatalytic activity of Pt/WO_3 and Au/WO_3 nanocomposites under sunlight-type excitation. *Solid State Sci.* **2011**, *13*, 1748–1754. [CrossRef]
55. Christopher, P.; Xin, H.; Linic, S. Visible-light-enhanced catalytic oxidation reactions on plasmonic silver nanostructures. *Nat. Chem.* **2011**, *3*, 467–472. [CrossRef]
56. Tahmasebi, N.; Mahdavi, S.M. Synthesis and optical properties of Au decorated colloidal tungsten oxide nanoparticles. *Appl. Surf. Sci.* **2015**, *355*, 884–890. [CrossRef]
57. Trasatti, S. The absolute electrode potential: An explanatory note (Recommendations 1986). *Pure Appl. Chem.* **1986**, *58*, 955–966. [CrossRef]
58. Ke, J.; Zhou, H.; Liu, J.; Duan, X.; Zhang, H.; Liu, S.; Wang, S. Crystal transformation of 2D tungstic acid H_2WO_4 to WO_3 for enhanced photocatalytic water oxidation. *J. Colloid Interface Sci.* **2018**, *514*, 576–583. [CrossRef]
59. Deng, X.; Dou, J.; Li, F.; Gao, H.; Liu, G. The Facile Hydrothermal Preparation of Orthorhombic WO_3 with (001) Facet and Its Photocatalytic Performance. *J. Nanosci. Nanotechnol.* **2015**, *15*, 9812–9817. [CrossRef]
60. Liang, Y.; Yang, Y.; Zou, C.; Xu, K.; Luo, X.; Luo, T.; Li, J.; Yang, Q.; Shi, P.; Yuan, C. 2D ultra-thin WO_3 nanosheets with dominant {002} crystal facets for high-performance xylene sensing and methyl orange photocatalytic degradation. *J. Alloy. Compd.* **2019**, *783*, 848–854. [CrossRef]
61. Hu, D.; Diao, P.; Xu, D.; Wu, Q. Gold/WO_3 nanocomposite photoanodes for plasmonic solar water splitting. *Nano Res.* **2016**, *9*, 1735–1751. [CrossRef]
62. Sarina, S.; Waclawik, E.R.; Zhu, H. Photocatalysis on supported gold and silver nanoparticles under ultraviolet and visible light irradiation. *Green Chem.* **2013**, *15*, 1814–1833. [CrossRef]
63. Adhikari, S.; Swain, R.; Sarkar, D.; Madras, G. Wedge-like WO_3 architectures for efficient electrochromism and photoelectrocatalytic activity towards water pollutants. *Mol. Catal.* **2017**, *432*, 76–87. [CrossRef]
64. Liu, J.; Zhorabek, F.; Zhang, T.; Lam, J.W.Y.; Tang, B.Z.; Chau, Y. Multifaceted Cargo Recruitment and Release from Artificial Membraneless Organelles. *Small* **2022**, *18*, e2201721. [CrossRef]
65. Singh, J.; Satpati, B.; Mohapatra, S. Structural, Optical and Plasmonic Properties of Ag-TiO_2 Hybrid Plasmonic Nanostructures with Enhanced Photocatalytic Activity. *Plasmonics* **2016**, *12*, 877–888. [CrossRef]
66. Chen, Z.; Fang, L.; Dong, W.; Zheng, F.; Shen, M.; Wang, J. Inverse opal structured Ag/TiO_2 plasmonic photocatalyst prepared by pulsed current deposition and its enhanced visible light photocatalytic activity. *J. Mater. Chem. A* **2013**, *2*, 824–832. [CrossRef]
67. Bian, Z.; Tachikawa, T.; Zhang, P.; Fujitsuka, M.; Majima, T. Au/TiO_2 Superstructure-Based Plasmonic Photocatalysts Exhibiting Efficient Charge Separation and Unprecedented Activity. *J. Am. Chem. Soc.* **2013**, *136*, 458–465. [CrossRef] [PubMed]
68. Rhaman, M.; Ganguli, S.; Bera, S.; Rawal, S.B.; Chakraborty, A.K. Visible-light responsive novel WO_3/TiO_2 and Au loaded WO_3/TiO_2 nanocomposite and wastewater remediation: Mechanistic inside and photocatalysis pathway. *J. Water Process. Eng.* **2020**, *36*, 101256. [CrossRef]
69. Ding, D.; Liu, K.; He, S.; Gao, C.; Yin, Y. Ligand-Exchange Assisted Formation of Au/TiO_2 Schottky Contact for Visible-Light Photocatalysis. *Nano Lett.* **2014**, *14*, 6731–6736. [CrossRef]

70. Zhang, Q.; Dong, R.; Wu, Y.; Gao, W.; He, Z.; Ren, B. Light-Driven Au-WO_3@C Janus Micromotors for Rapid Photodegradation of Dye Pollutants. *ACS Appl. Mater. Interfaces* **2017**, *9*, 4674–4683. [CrossRef]
71. Ustun, O.; Yilmaz, A.; Yilmaz, M. Catalytic and SERS activities of WO_3-based nanowires: The effect of oxygen vacancies, silver nanoparticle doping, and the type of organic dye. *Phys. Chem. Chem. Phys.* **2022**, *24*, 18615–18626. [CrossRef]
72. Chen, H.; Yu, X.; Zhu, Y.; Fu, X.; Zhang, Y. Controlled synthesis of {001} facets-dominated dye-sensitized BiOCl with high photocatalytic efficiency under visible-light irradiation. *J. Nanopart. Res.* **2016**, *18*, 1–13. [CrossRef]
73. Zang, L.; Liu, C.-Y.; Ren, X.-M. Photochemistry of semiconductor particles 3. Effects of surface charge on reduction rate of methyl orange photosensitized by ZnS sols. *J. Photochem. Photobiol. A Chem.* **1995**, *85*, 239–245. [CrossRef]
74. Liu, J.; Xu, S.-M.; Li, Y.; Zhang, R.; Shao, M. Facet engineering of WO_3 arrays toward highly efficient and stable photoelectrochemical hydrogen generation from natural seawater. *Appl. Catal. B Environ.* **2019**, *264*, 118540. [CrossRef]